# Coarse predictions of dipole reversals by low-dimensional modeling and data assimilation

Matthias Morzfeld, Alexandre Fournier, Gauthier Hulot

Physics of the Earth and Planetary Interiors 262 (2017) 8–27

Contents lists available at ScienceDirect

Physics of the Earth and Planetary Interiors

journal homepage: www.elsevier.com/locate/pepi

# Coarse predictions of dipole reversals by low-dimensional modeling and data assimilation

Matthias Morzfeld [a,*], Alexandre Fournier [b], Gauthier Hulot [b]

[a] Department of Mathematics, University of Arizona, 617 N. Santa Rita Ave., P.O. Box 210089, Tucson, AZ 85721-0089, USA
[b] Institut de Physique du Globe de Paris, Sorbonne Paris Cité, Université Paris Diderot, CNRS, 1 Rue Jussieu, 75005 Paris, France

ARTICLE INFO

*Article history:*
Received 22 July 2016
Received in revised form 10 October 2016
Accepted 17 October 2016
Available online 22 October 2016

ABSTRACT

Low-dimensional models for Earth's magnetic dipole may be a powerful tool for studying large-scale dipole dynamics over geological time scales, where direct numerical simulation remains challenging. We investigate the utility of several low-dimensional models by calibrating them against the signed relative paleointensity over the past 2 million years. Model calibrations are done by "data assimilation" which allows us to incorporate nonlinearity and uncertainty into the computations. We find that the data assimilation is successful, in the sense that a relative error is below 8% for all models and data sets we consider. The successful assimilation of paleomagnetic data into low-dimensional models suggests that, on millennium time scales, the occurrence of dipole reversals mainly depends on the large-scale behavior of the dipole field, and is rather independent of the detailed morphology of the field. This, in turn, suggests that large-scale dynamics of the dipole may be predictable for much longer periods than the detailed morphology of the field, which is predictable for about one century. We explore these ideas and introduce a concept of "coarse predictions", along with a sound numerical framework for computing them, and a series of tests that can be applied to assess their quality. Our predictions make use of low-dimensional models and assimilation of paleomagnetic data and, therefore, rely on the assumption that currently available paleomagnetic data are sufficiently accurate, in particular with respect to the timing of reversals, to allow for coarse predictions of reversals. Under this assumption, we conclude that coarse predictions of dipole reversals are within reach. Specifically, using low-dimensional models and data assimilation enables us to reliably predict a time-window of 4 kyr during which a reversal will occur, without being precise about the timing of the reversal. Indeed, our results lead us to forecast that no reversal of the Earth's magnetic field is to be expected within the next few millennia. Moreover, we confirm that the precise timing of reversals is difficult to predict, and that reversal predictions based on intensity thresholds are unreliable, which highlights the value of our model based coarse predictions.



## 1. Introduction

Earth possesses a time-varying magnetic field which is generated and sustained against Ohmic decay by a fluid dynamo driven by convection in its interior. The geomagnetic field changes over a wide range of time scales, from years to millions of years, and its strongest component, the dipole, has the dramatic feature that it occasionally switches polarity, i.e. the geomagnetic North becomes South, and vice versa (see, e.g., Hulot et al., 2010a). Such reversals happened throughout the geological history of our planet and their occurrence is well documented over the past 150 million years (Cande and Kent, 1995; Lowrie and Kent, 2004). However, little is known about the mechanisms that lead to a reversal. For example, detailed changes in the geometry of the geomagnetic field during a reversal are still poorly documented, and the conditions under which the reversal is initiated in Earth's core remain essentially unknown (see, e.g., Amit et al., 2010; Glatzmaier and Coe, 2015; Valet and Fournier, 2016, for recent reviews).

A direct approach to modeling the geomagnetic field is numerical simulation of rapidly rotating spherical fluid shells, such as Earth's fluid outer core, where the dynamo is operating. The computational cost of this approach is large, in particular if one wants to study the dipole over geological time scales of millions of years, so that only investigations with relatively limited dynamo simulations could be used so far (see, e.g., Lhuillier et al., 2013; Olson et al., 2013; Wicht and Meduri, 2016). An alternative to direct numerical modeling is low-dimensional modeling. The idea is to derive a simplified representation of the large scale dynamics of a complex system while neglecting smaller scales. Several

* Corresponding author.
*E-mail address:* mmo@math.arizona.edu (M. Morzfeld).

http://dx.doi.org/10.1016/j.pepi.2016.10.007
0031-9201/

low-dimensional models have already been proposed for cloud modeling (Koren and Feingold, 2011; Feingold and Koren, 2013) and for modeling of Earth's dipole (Rikitake, 1958; Nozières, 1978; Hoyng et al., 2001; Brendel et al., 2007; Pétrélis and Fauve, 2008; Pétrélis et al., 2009; Kuipers et al., 2009; Gissinger et al., 2010; Gissinger, 2012; Buffett et al., 2013; Buffett et al., 2014; Buffett and Matsui, 2015; Buffett, 2015; Meduri and Wicht, 2016). In the context of Earth's magnetic field, a low-dimensional model represents the effects of complex interaction of the magnetic field and fluid flow, however the details of these interactions are not resolved. The heuristic arguments for the validity of these models are that the magnetic diffusivity is larger than the kinematic viscosity by several orders of magnitude, which implies that the small-scale magnetic field, induced by small-scale velocity modes, is strongly damped, and, thus, the dynamics are dominated by a few magnetic modes (Gissinger, 2012). However, work that investigates the "usefulness" of low-dimensional models quantitatively is still missing. Here,"useful" is to be understood in the sense that low-dimensional models can reproduce paleomagnetic data, and that the models produce reliable predictions of large scale dynamics. Indeed, one of the main goals of this paper is to establish a suitable set of tests that can be used to quantify the utility of low-dimensional models for the geodynamo.

We present a data-driven, Bayesian approach and we calibrate the models against paleomagnetic data by "data assimilation", i.e., we estimate model states from data by Bayesian statistics (see, e.g., Chorin and Hald, 2013). The data are the signed relative paleointensities which provide estimates of the strength of the axial dipole and its polarity over the past 2 Myr. The relative paleointensity is provided by Sint-2000 (Valet et al., 2005) and PADM2M (Ziegler et al., 2011) data sets, the polarity can be derived from the geomagnetic polarity time scale (Cande and Kent, 1995; Lowrie and Kent, 2004). We consider four low-dimensional models:

(i) the deterministic three-variable model presented in Gissinger (2012), which we call G12;
(ii) the stochastic model presented in Buffett et al. (2013), which we refer to as B13;
(iii) the stochastic model derived in Pétrélis et al. (2009), which we abbreviate by P09;
(iv) a new scalar stochastic model that combines the numerical techniques used in Buffett et al. (2013) with the G12 model; we call this model the G12 based SDE.

Our data assimilation results (Section 3) indeed establish compatibility of models and data in the sense that an average error after assimilation is no larger than 8% for all models and data sets we tried, provided that suitable numerical techniques are used. This result is robust to variations in how the data are assimilated or how the data were obtained, since we obtain quantitatively similar results with several numerical data assimilation methods (see Appendix B) and with both data sets.

The compatibility of low-dimensional models and paleomagnetic data suggests that general conditions for reversals to occur mainly result from the large-scale behavior of the dipole field, with the detailed morphology of the field playing a role only once such general conditions are met. If this were indeed the case, one could predict the large-scale dipole field over long time-scales, perhaps several thousand years. We investigate this possibility in Section 4 where we introduce the concept of "coarse predictions" for dipole reversals. Specifically, we determine if we can identify *time-windows* of a few millennia during which reversals are likely to occur, without being precise about the timing of reversals within the time-windows. The temporal horizon of our predictions is comparable to the time needed for a reversal to occur, but shorter than the typical time elapsed between reversals. Coarse predictions could thus provide an "early warning system", indicating that a reversal might occur within the next few millennia.

We present a series of tests to investigate if our proposed framework, which relies on low-dimensional models and data assimilation, produces more reliable predictions than several purely data-based prediction strategies. Predictions obtained in this way rely on the assumption that the paleomagnetic data, as documented by Sint-2000 and PADM2M, (one data point every 1000 years) are sufficiently accurate for this purpose. Conditional on the latter assumption, we conclude that coarse predictions are indeed within reach, even with simple low-dimensional models. This highlights the value of low-dimensional models and data assimilation as an effective tool for addressing questions that are difficult to answer by other techniques, in particular direct numerical modeling. Perhaps more importantly, the coarse predictions we present, and the series of tests we suggest, may be useful to assess the utility of a future generations of improved low- or "intermediate"-dimensional models.

## 2. Paleomagnetic data and low-dimensional models

### 2.1. Paleomagnetic data

The data we use are the signed relative paleointensity of the past 2 Myr. These intensities describe estimates of the strength of the axial dipole, and are available in the Sint-2000 (Valet et al., 2005) and PADM2M (Ziegler et al., 2011) data sets with a 1 kyr time step. The polarity is encoded by the sign of the dipole, which is taken from the geomagnetic polarity time scale (Cande and Kent, 1995; Lowrie and Kent, 2004). To find the exact timing of the polarity changes we proceed in slightly different ways for Sint-2000 and PADM2M. In the case of Sint-2000, we assume that reversals occur at time of polarity changes as confirmed from inspection of the original directional information of Valet et al. (2005) (J.P. Valet, personal communication). In the case of PADM2M, however, we do not have access to analogous directional information. We therefore a priori assumed the same timing as for Sint-2000, and checked that reversals did correspond to a minimum in the intensity record provided by PADM2M to within 1kyr. This turned out to be the case for most reversals, except for the Bruhnes Matuyama reversal and the two reversals bounding the Cobb mountain subchron. For these three reversals, a slight time shift was introduced to reconcile their timing with that of intensity lows in PADM2M, resulting in slight shifts in the timing of the sign changes in the PADM2M signed relative paleointensity with respect to that of Sint-2000.

For each data set, a unit relative paleointensity corresponds to a virtual axial dipole moment of $7.46\ 10^{22}$ $Am^2$, as in Valet et al. (2005). Both data sets contain the relative paleointensity along with a Gaussian error model, i.e., every 1 kyr a datum of the paleointensity is available along with an estimated standard deviation. However, the standard deviations of PADM2M are significantly smaller than those of Sint-2000. While the small errors of PADM2M may be accurate representations of the "pure" data error, they seem unreasonably small in the context of data assimilation. The reason is that these errors must describe a combination of "measurement errors", i.e., the uncertainty of the data, and "model errors", i.e., how good the (low-dimensional) model is. We thus adjust the errors in PADM2M to account for model error. In the data assimilation (see Section 3) we use the Sint-2000 standard deviations for the PADM2M data. In particular, we find that the data assimilation is more stable with the larger standard deviations of Sint-2000. Fig. 1 shows the mean and 95% confidence interval of the Sint-2000 data as well as the mean of PADM2M.

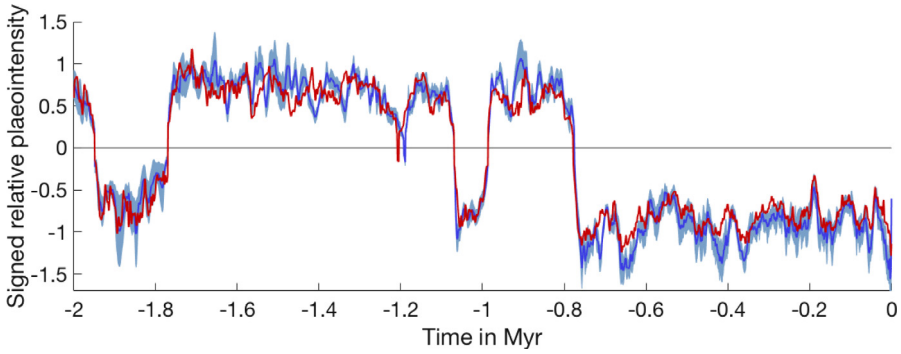


**Fig. 1.** Signed relative paleointensity. The blue line represents the signed Sint-2000 data (Valet et al., 2005) and the light blue cloud represents a 95% confidence interval. The red line represents the mean of the PADM2M data (Ziegler et al., 2011). (For interpretation of the references to colour in this figure legend, the reader is referred to the web version of this article.)

### 2.2. Scalar stochastic differential equation models: P09 and B13

The P09 (Pétrélis et al., 2009) and B13 (Buffett et al., 2013) models are stochastic differential equations (SDE) of the form

$$\mathrm{d}x = f(x)\mathrm{d}t + g(x)\mathrm{d}W, \tag{1}$$

where the state, $x$, is either directly or indirectly related to the geomagnetic dipole, $f(x)$ and $g(x)$ are scalar functions, $W$ is a Brownian motion, and $t$ is time. A Brownian motion has the characteristics that it is almost surely continuous everywhere, that increments are independent Gaussian random variables $W(t) - W(s) \sim \mathcal{N}(0, s-t)$, and that $W(0) = 0$. Here and below, $\mathcal{N}(\mu, \sigma^2)$ is our notation for a Gaussian random variable with mean $\mu$ and variance $\sigma^2$. The two models differ in their functions $f(x)$ and $g(x)$ and in the way $x$ is related to the geomagnetic dipole.

The B13 model (Buffett et al., 2013) postulates that the dipole dynamics are governed by an SDE of the form (1), for which the state $x$ is the geomagnetic dipole, and where the Brownian motion describes the effects of turbulent fluctuations of a velocity field. The drift and diffusion coefficients, $f(x)$ and $g(x)$, are estimated from paleomagnetic data. Specifically, the drift is derived from a double-well potential, i.e., Earth's dipole is modeled by a particle in a double-well, where each well represents a polarity. The particle, located in one of the wells, gets pushed around by noise, and the effects of the noise may push the particle to overcome the potential barrier, thus completing a reversal of the dipole. In Buffett et al. (2013), the drift and diffusion coefficients are estimated from Sint-2000 and PADM2M. Below we use the one resulting from PADM2M, and refer to Buffett et al. (2013) for the details of the numerics and their tuning. Since the drift and diffusion parameters are estimated from paleomagnetic data, the variable $t$ of the resulting SDE model is "automatically" scaled as time. A typical simulation with B13 is shown in the upper-left panel of Fig. 2.

The B13 model has been used in other contexts as well. In Buffett et al. (2014), the same stochastic modeling approach was applied to data from numerical dynamo models, and in Buffett and Matsui (2015), the stochastic term of the B13 model was modified to account for correlations in time. Buffett (2015) used yet another variant of this model to study reversal duration and the intensity of fluctuations during a reversal. A model similar to the B13 model has also been discussed by Hoyng et al. (2001), and later by Brendel et al. (2007) and Kuipers et al. (2009), who relied on a different numerical method to estimate the drift and diffusion coefficients. However, the details of how the drift and diffusion coefficients are computed are not important for our purposes. Finally, we note that the B13 model was recently revisited by Meduri and Wicht (2016), who relied on numerical dynamo simulations and paleomagnetic data to build SDE models of the form (1).

The P09 model (Pétrélis et al., 2009) is based on the assumption that a general mechanism for field reversals exists, and that this process is largely independent of the details of the velocity field. Specifically, the model describes the interaction of two modes of comparable thresholds, i.e., the magnetic field is $B(r,t) = a(t)B_1(r) + b(t)B_2(r)$. By imposing the symmetry of the equations of magnetohydrodynamics $B \to -B$ in the amplitude equation, and by assuming that the amplitude has a shorter time scale than the phase, one obtains an SDE for the phase of the form (1) with

$$f(x) = \alpha_0 + \alpha_1 \sin(2x), \quad g(x) = 0.2\sqrt{|\alpha_1|}. \tag{2}$$

The dipole can be calculated from this phase by $D = R\cos(x + x_0)$. We use the same parameters as in Pétrélis et al. (2009), $\alpha_1 = -185\,\mathrm{Myr}^{-1}, \alpha_0/\alpha_1 = -0.9, x_0 = 0.3$. This choice of parameters also defines a time-scale for the variable $t$. Regarding the amplitude of the dipole, we set $R = 1.3$ to scale the P09 model output to have the same average relative paleointensity as the unsigned Sint-2000 data. With these parameters, the model exhibits abrupt reversals and large fluctuations, as shown in the upper-right panel of Fig. 2, where a typical simulation result of P09 is shown.

The mechanism for reversals in the P09 model is as follows. The model has four fixed points, two are stable, and two are unstable. The two stable fixed points represent the two dipole polarities (North–South/South-North). The system hovers around one of the stable fixed points and gets pushed around by the noise (the Brownian motion), which represents the effects of turbulent fluctuations. When the deviation from the stable fixed point becomes large, the state can move beyond the neighboring unstable fixed point and then is attracted by the opposite stable fixed point, and a reversal of the dipole is completed. A more detailed discussion of the rich dynamics of this system is given in Pétrélis et al. (2009).

### 2.3. The deterministic G12 model and the G12 based SDE model

The G12 model consists of three deterministic ordinary differential equations (ODE),

$$\frac{dQ}{dt} = \mu Q - VD, \quad \frac{dD}{dt} = -\nu D + VQ, \quad \frac{dV}{dt} = \Gamma - V + QD, \tag{3}$$

where $t \geqslant 0$ is to be identified as time, and where $\mu, \nu$ and $\Gamma$ are scalar parameters, see Gissinger (2012). In this model $Q$ represents the quadrupole, which may play an important role during reversals (McFadden et al., 1991; Glatzmaier and Roberts, 1995), $D$ is the

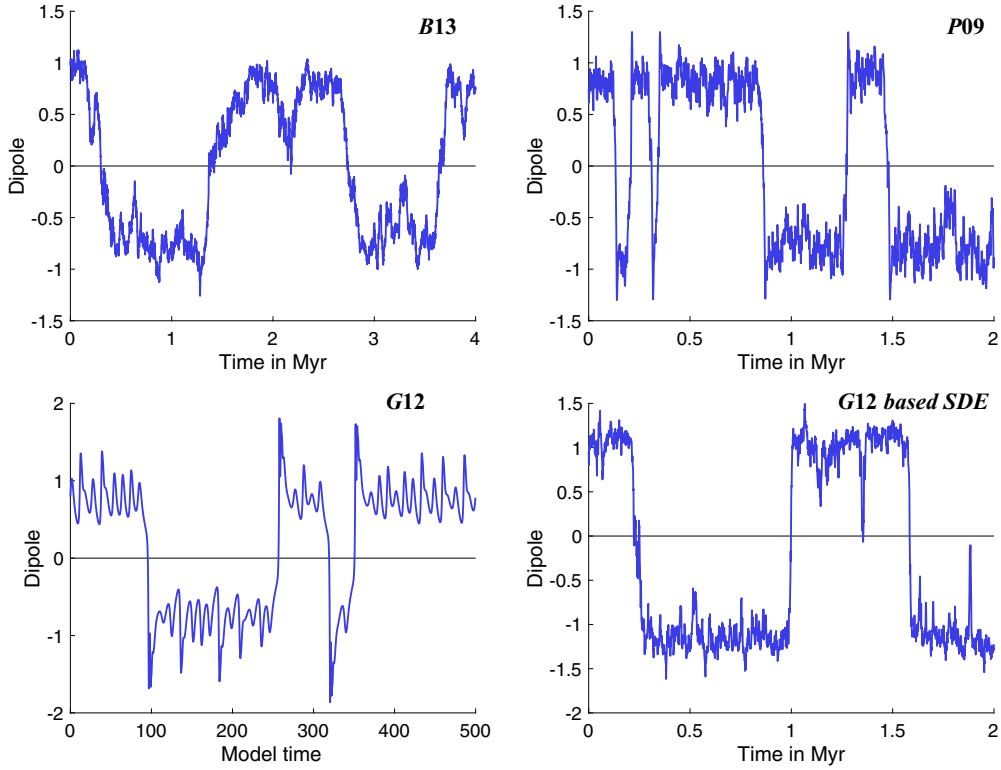


**Fig. 2.** Dipole simulations with low-dimensional models. Top row: B13 (left) and P09 (right). Bottom row: G12 (left) and G12 based SDE (right). "Time" in the lower left panel is dimensionless.

dipole and $V$ represents the flow, more specifically, its equatorially-antisymmetrical component (e.g., Gubbins and Zhang (1993)). The rich dynamics of these equations are studied by Gissinger (2012). In particular, it is shown that reversals are generated by crisis-induced intermittency when $\mu = 0.119, \nu = 0.1$, and $\Gamma = 0.9$ and that the model then shares a number of characteristics with the paleomagnetic data.

*2.3.1. Scaling of G12*

The G12 model is not equipped with a natural scaling of the amplitude of the dipole variable $D$ to the geomagnetic dipole amplitude, or with a scaling of G12 model time, $t$, to geophysical time. To find the amplitude scaling of G12 we compute, as before, the average relative paleointensity of the unsigned Sint-2000 and PADM2M data sets and also compute the average of the absolute value of the dipole variable of ten G12 model runs for 250 dimensionless time units. By setting

G12 amplitude scaling :

$$D = \sqrt{2} \times \text{relative paleointensity (signed)},$$

the average of the G12 dipole variable is approximately equal to the average relative paleointensity. Moreover, this scaling leads to good agreement of the histograms of the dipole variable $D$ and of the signed relative paleointensity of Sint-2000 and PADM2M (left panel of Fig. 3). A typical simulation with G12 is shown in the lower left panel of Fig. 2.

To find the scaling of G12 model time, we may use the fact that the distribution of chron duration, i.e., the distribution of the time periods during which the geomagnetic dipole is in a stable polarity, is well approximated by a gamma distribution for both the paleomagnetic data (Lowrie and Kent, 2004; Cande and Kent, 1995) and the G12 model, as shown by Gissinger (2012). By matching the shape parameters of a gamma distribution from G12 simulation data with the shape parameters of a gamma distribution of the paleomagnetic chron durations, we derive the

G12 geological time scale :

1unit of G12 dimensionless model time = 1 kyr.

The shape parameters are computed by maximum likelihood estimation. For the paleomagnetic chron durations, these parameters are estimated from the CK95(1) data set of Cande and Kent (1995) as defined in Lowrie and Kent (2004), which contains the sign of the dipole over the past 30 Myr. For the G12 model, the parameters are estimated from ten simulation for $10^4$ dimensionless time units. The right panel of Fig. 3 shows histograms and corresponding gamma distributions for CK95(1) and G12 when using this geological time scale.

It is instructive to assess this scaling by comparing the power spectral densities of G12 simulation data and Sint-2000/PADM2M data. We compute these spectra by the multi-taper spectral estimation technique described in Constable and Johnson (2005). The spectra are shown in the left panel of Fig. 4. Note that the first corner frequencies of the G12 model and of the Sint-2000 and PADM2M data match, but that the G12 model has a larger high-frequency content than PADM2M or Sint-2000 (by roughly one order of magnitude for frequencies of 2 $\text{Myr}^{-1}$ and above). We can attribute the low-frequencies to the occurrence of reversals, and the high frequencies to millennium scale dipole variations during chrons. This suggests that, when scaled using the above geological time scale, the dynamics of G12 essentially match the reversal statistics of the geomagnetic dipole, but fail to match its millennium behavior. We note that the high frequency content of Sint-2000 and PADM2M could be underestimated because the data are obtained by averaging over stacks, which possibly smoothes the signal. Indeed, Constable and Johnson (2005) constructed a spectral model whose high-frequency content is also larger than

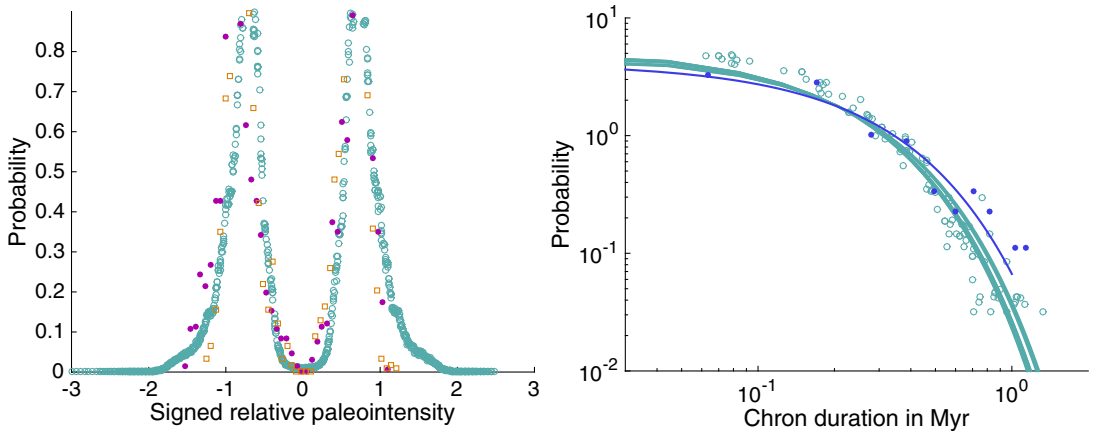


**Fig. 3.** Left: histogram of signed relative paleointensity of Sint-2000 (purple dots), PADM2M (orange squares) and G12 after amplitude scaling (turquoise circles). Right: histogram of the chron duration over the past 30 Myr (blue dots, data from the CK95(1) (Cande and Kent, 1995) data set) and the maximum-likelihood gamma distribution fit (blue line); also shown are a histogram of G12 simulation data scaled using the geological time scale of 1 unit = 1kyr (turquoise circles) and maximum-likelihood fits for gamma distributions for each run (turquoise lines). See also Figs. 13 and 12 in Gissinger (2012). (For interpretation of the references to colour in this figure legend, the reader is referred to the web version of this article.)

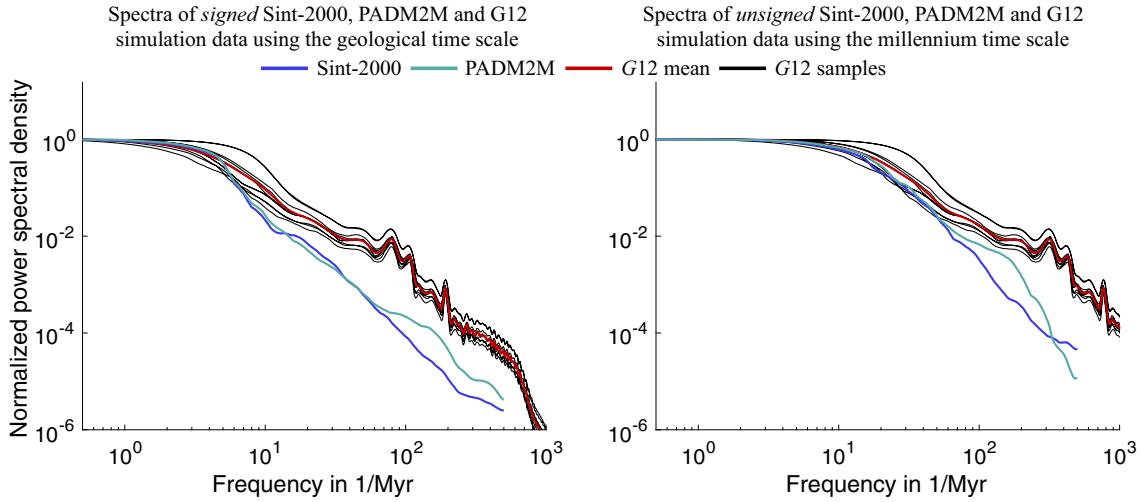


**Fig. 4.** Left: spectra of Sint-2000 (blue), PADM2M (turquoise) and G12 (red, average of 10 model runs of $10^4$ time units, each in black) when scaling to the geological time scale of 1 unit = 1kyr. Right: spectra of Sint-2000 (blue), PADM2M (turquoise) and G12 (red, average of 10 model runs of $10^4$ time units, each in black) when scaling to the millennium time scale of 1 unit = 4kyr. (For interpretation of the references to colour in this figure legend, the reader is referred to the web version of this article.)

that of PADM2M or Sint-2000. However, we also note that the above geological time scale was computed using reversal statistics over the past 30 Myr, a period during which the reversal rate has increased by a factor of about 2 (see, e.g., Gallet and Hulot (1997)). A geological time scale estimated from more recent epochs would have been larger.

The mismatch of model and data for high-frequencies suggests that the geological time scale may not be optimal for scaling the G12 model, in particular because the G12 model cannot be scaled to simultaneously match the geological and millennium dynamics of the Earth's dipole field. This can be further illustrated by comparing spectra of *unsigned* data, shown in the right panel of Fig. 4. The low frequencies of the spectra of unsigned data are no longer dominated by reversal frequencies, with reversals occurring over millions of years, but are rather representative of field variations over millennia. By comparing spectra of unsigned data, we find that matching the millennium scale of Earth's dynamics to the "millennium" variation of the G12 model requires a timescale four times larger than when matching model time to geological time scale. We thus define the

G12 millenium time scale :

1unit of G12 dimensionless model time = 4 kyr.

In our attempts to assimilate data in the G12 model (see Section 3), we observe that results improve dramatically when this millennium time scale is used, rather than the geological time scale, independently of the numerical data assimilation technique we use. This is an important observation. The reason is that reversals are rare, there are only 7 reversals within the 2000 data points we consider. This implies that an accurately represented millennium variation is more important for successful data assimilation than an accurate representation of the average time elapsed between reversals, i.e., the geological time scale. Indeed, with our millennium time scale, the G12 model encouragingly captures much of the behavior of the dipole before and during a reversal (left panel of Fig. 5). For the rest of this paper, we thus only use the millennium time scale.

Fig. 5 illustrates the typical reversing behavior of the G12 model. We observe that the dipole slowly decreases and then quickly reverses, as is also observed in all reversals of the Sint-

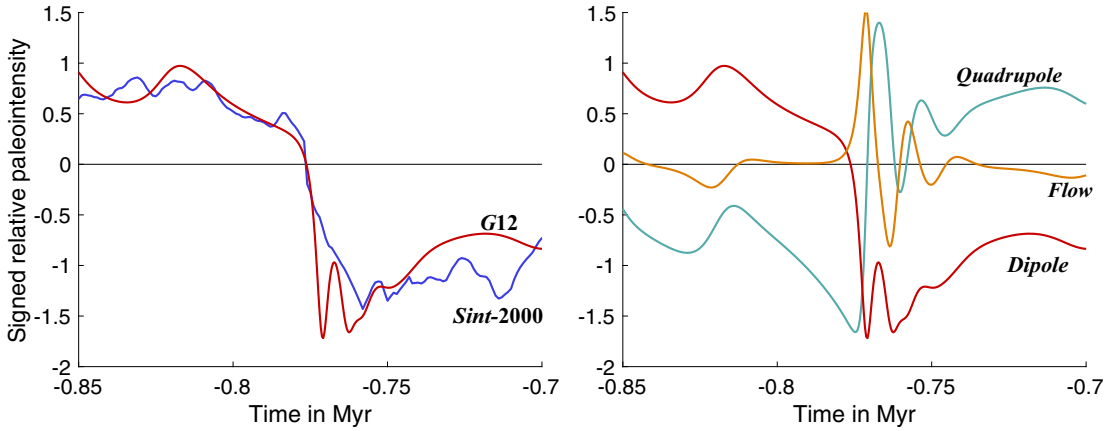


**Fig. 5.** Left: Example reversal in a free run of the G12 model (red) scaled to the millennium time scale (1 unit = 4 kyr) and artificially synchronized to the time of the Brunhes–Matuyama reversal as seen in the Sint-2000 data (blue). Right: Behavior of the dipole (red), flow (yellow), quadrupole (turquoise) parameters of the G12 model during that same reversal (see also Gissinger, 2012). The amplitude of the G12 model state variables $D, Q$, and $V$ has been scaled by the factor $1/\sqrt{2}$. (For interpretation of the references to colour in this figure legend, the reader is referred to the web version of this article.)

2000 data. The dipole reversal is followed by an overshoot, and such overshoots, perhaps less pronounced, are also observed in the data (Valet et al., 2005). The right panel of Fig. 5 further illustrates the behavior of the flow and quadrupole variables during a dipole reversal. Specifically, when the dipole decreases, the quadrupole variable increases, and then reverses with the dipole. A strong peak can be observed in the velocity during a reversal.

Another dynamic time scale worth looking into is the $e$-folding time of the G12 model. This $e$-folding time is defined as the time it takes for the "distance" between two G12-trajectories to be multiplied by a factor $e$, and is an indicator of the intrinsic predictability of the G12 model. Its average value is estimated to be around 40 kyr (see Appendix A). This is much larger than the 30 year $e$-folding time found in three-dimensional simulations, which must also account for the complex and fast-evolving non-dipole field (Hulot et al., 2010b; Lhuillier et al., 2011a). Provided that the G12 model can provide a useful coarse representation of the Earth's dipole field with only three variables, this thus suggests that the G12 model could indeed be used to predict the average dipole field evolution over time-scales of several kyr. Such "coarse" predictions are precisely what we aim at, and they may not be limited by the short predictability of the detailed evolution of the full 3D field. We investigate these ideas in more detail in Section 4.

#### 2.3.2. G12 based SDE

We further use the G12 model to propose an additional scalar SDE model, similar to the B13 model. We mimic the construction of the B13 model, but substitute the paleomagnetic data (Sint-2000 or PADM2M) with synthetic data from G12 scaled to the millennium scale as described above. In constructing a G12 based SDE model, we postulate an SDE (1) for the dipole of the G12 model and use the numerical techniques of Buffett et al. (2013) to estimate the drift and diffusion coefficients from G12 simulation data (rather than from paleomagnetic data). Specifically, we fit a cubic function to the drift and a quadratic function to the square root of the diffusion coefficient. We refer to this model as the "G12 based SDE". A typical simulation with the G12 based SDE is shown in the lower right panel of Fig. 2.

## 3. Data assimilation results

We perform data assimilation using the various numerical methods described in appendix B and the two data sets Sint-2000 and PADM2M. For each model, data set and data assimilation technique, we compute the relative error of the assimilation over the 2 Myr period defined by

$$e = \frac{\sum_{n=1}^{2000}\left(z^n - \widehat{E}\left[x^n \mid z^{1:n}\right]\right)^2}{\sum_{n=1}^{2000}\left(z^n\right)^2}, \tag{4}$$

where $z^n$ are the data at time $n$ kyr and $\widehat{E}\left[x^n \mid z^{1:n}\right]$ is the approximation of the conditional mean of the dipole given the data up to time $n$ kyr. The conditional mean is the minimum mean square error estimate of the state, see, e.g., Chorin and Hald (2013). Each method resorts to a finite number of model samples, also called particles, whose distribution aims at providing a faithful description of the model uncertainties. For each method, we vary the number of samples from 50 to 400, compute the above error, and check that sampling error is not the dominating error. In all cases, we observe that the error decreases when we increase the number of samples, but not by much, which indicates that 200–400 samples are sufficient to compute reliable estimates by Monte Carlo.

### 3.1. Data assimilation with scalar SDE models

We first consider the three scalar SDE models B13, G12 based SDE, and P09. We apply the ensemble Kalman filter for stochastic models (S-EnKF), sequential data assimilation with implicit sampling (S-IMP) and sequential importance sampling with resampling (SIR) to these models (see Section B.2 in appendix B for a brief description of each method). For the P09 model we only used the SIR method. The reason is that the P09 model is "more nonlinear" than the B13 or G12 based SDE models, which makes the implementation of the other techniques more difficult. However, EnKF and S-IMP are techniques to keep the computational requirements of data assimilation reasonable and, since computation is not an issue here, using SIR is feasible. In each method, we use one observation per assimilation sweep. The results are listed in Table 1. Typical results of data assimilation by the G12 based SDE and P09 model are shown in the left and right panels of Fig. 6. A typical result obtained by B13 is qualitatively similar.

For the B13 and G12 based SDE models, and using suitable numerical data assimilation, both data sets lead to errors no larger than 6%. Errors are only slightly larger in the case of the P09 model. Such small errors suggest that the "free dynamics" of the scalar models are, in principle, compatible with that of the geomagnetic

**Table 1**
Relative error (in %) of paleomagnetic data assimilation. We assimilate Sint-2000 and PADM2M into B13, G12 based SDE and P09 by S-EnKF, SIR and S-IMP, and into G12 by D-EnKF and D-IMP (see appendix B.2). We vary the number of samples to check that sampling error is not the dominating error and vary the number of data points used per assimilation sweep for G12 in D-IMP.

| | | B13 | | | G12 based SDE | | | P09 | | G12 | | | |
|---|---|---|---|---|---|---|---|---|---|---|---|---|---|
| | Method: | S-EnKF | SIR | S-IMP | S-EnKF | SIR | S-IMP | SIR | D-EnKF | D-IMP | | | |
| | Data/sweep: | 1 | 1 | 1 | 1 | 1 | 1 | 1 | 1 | 1 | 5 | 10 | 15 |
| | # samples | | | | | | | | | | | | |
| Sint-2000 | 50 | 5.61 | 6.72 | 5.91 | 2.57 | 2.94 | 2.64 | 7.91 | 30.5 | 5.70 | 3.74 | 4.28 | 10.90 |
| | 100 | 5.46 | 6.37 | 5.76 | 2.31 | 2.64 | 2.53 | 7.29 | 30.7 | 5.43 | 3.80 | 4.20 | 10.93 |
| | 200 | 5.53 | 6.25 | 5.65 | 2.37 | 2.57 | 2.48 | 7.83 | 30.0 | 5.38 | 3.61 | 6.19 | 10.91 |
| | 400 | 5.46 | 6.10 | 5.63 | 2.32 | 2.51 | 2.51 | 7.35 | 29.5 | 5.39 | 3.51 | 6.18 | 10.88 |
| PADM2M | 50 | 5.37 | 8.03 | 5.39 | 2.15 | 2.47 | 2.22 | 9.06 | 27.1 | 6.63 | 5.09 | 5.98 | 10.7 |
| | 100 | 5.23 | 8.27 | 5.28 | 1.93 | 2.18 | 2.07 | 8.84 | 27.9 | 6.27 | 4.92 | 5.93 | 10.5 |
| | 200 | 5.23 | 7.51 | 5.27 | 1.72 | 2.08 | 1.91 | 8.94 | 26.5 | 5.99 | 4.99 | 5.93 | 10.9 |
| | 400 | 5.22 | 7.42 | 5.20 | 1.68 | 2.05 | 1.82 | 8.46 | 26.8 | 5.83 | 4.92 | 5.83 | 10.7 |

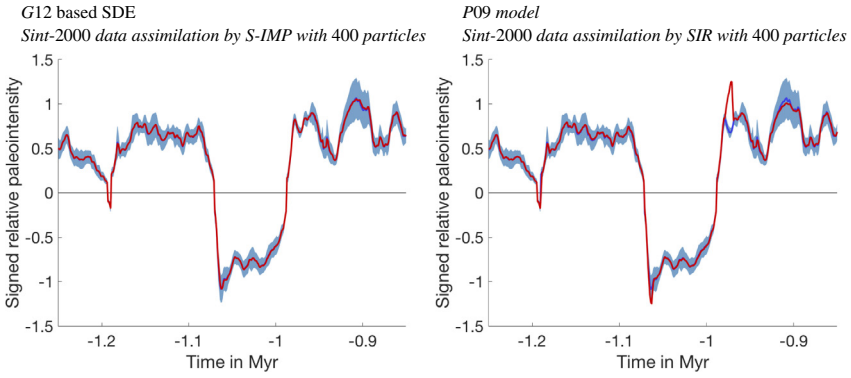


**Fig. 6.** Assimilation of Sint-2000 data into G12 based SDE by the S-IMP method with 400 samples (left) and assimilation of Sint-2000 data into P09 model by the SIR method with 400 samples (right). Blue: Sint-2000 data. Light blue cloud: Sint-2000 data 95% confidence interval. Red: conditional mean obtained through the assimilation process. (For interpretation of the references to colour in this figure legend, the reader is referred to the web version of this article.)

dipole, in the sense that data assimilation can keep the model trajectories close to the data.

This positive result is perhaps not surprising for B13 and P09, because the parameters of these models are adjusted to match paleomagnetic data. Specifically, drift and diffusion coefficients of the B13 model are estimated from the PADM2M data we assimilate, and the model parameters of the P09 model are chosen to "fit paleomagnetic data" (Pétrélis et al., 2009). However, the parameters that define the G12 based SDE are not estimated from these data. Rather, the drift and diffusion coefficients that define the G12 based SDE model are estimated from "synthetic data" of the G12 model (with model-time appropriately scaled, see above). The small errors we obtain with the G12 based SDE thus imply that G12 itself may be compatible with the paleomagnetic data. We study this in more detail below.

### 3.2. Data assimilation with G12

We now consider the deterministic G12 model and use the EnKF for deterministic models (D-EnKF) and sequential data assimilation with implicit sampling for deterministic models (D-IMP) to assimilate the PADM2M and Sint-2000 data. The D-EnKF and D-IMP techniques are described in detail in section B.1 of appendix B. When considering sequential data assimilation with implicit sampling, we can vary the number of data points we assimilate per sweep (see appendix B.1.2). Specifically, one can attempt to assimilate the 2 Myr of data in one sweep, i.e., one can try to find initial conditions for G12 that lead to a trajectory of the dipole variable that is compatible with the paleomagnetic data. However, this approach did not prove successful because the optimization required for implicit sampling failed to converge. The reasons for this failure are that (*i*) the G12 model cannot account simultaneously for the millennium and geological time scales of dipole fluctuations, whereas an assimilation over 2 Myr of data in one sweep assumes that both time scales are correctly represented (see Section 2.3.1); and (*ii*) the *e*-folding time of the G12 model of about 40 kyr makes it numerically difficult to propagate information from data backwards over several million years. To address these difficulties, we apply data assimilation sequentially as described in Appendix B.1.2. Specifically, we assimilate 1–15 kyr of data per sweep. The results are shown in Table 1. A typical result of data assimilation with G12 is shown in the top-left panel of Fig. 7. We observe that we obtain similar errors when assimilating 1 or 5 data points per sweep, however the assimilation result is a lot smoother when we use 5 data points per sweep. We further observe that the error increases steeply if more than 5 kyr of data are assimilated per sweep. Further, we observe that EnKF yields a larger error than implicit sampling. The reason may be that G12 is more nonlinear than the B13 model or the G12 based SDE model, in particular due to the $Q$ and $V$ variables. This makes the use of a nonlinear data assimilation method more important, because the Gaussian approximation of EnKF may not be valid.

It is evident from Fig. 7, that significant discontinuities occur at each time we assimilate data, i.e., every 5 kyr. These discontinuities indicate that assimilating the next 5 kyr of data has a large effect on the state estimate. This could be due to either an intrinsic incompatibility of the G12 model with the data, or large errors in the unobserved quadrupole and flow variables. We investigate this issue by using synthetic data shown in Fig. 8, generated as follows. We simulate the G12 model starting from initial conditions that

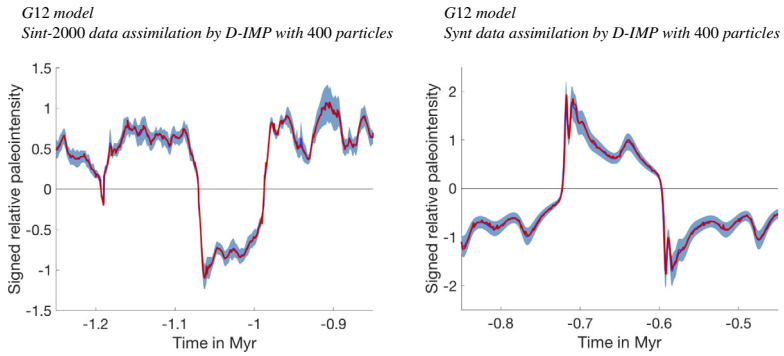


**Fig. 7.** Result of data assimilation (red) and data (blue, often hidden), along with assumed errors in the data (light blue cloud). Left: Sint-2000 data. Right: synthetic data (Synt, see text and Fig. 8). Data assimilation is done by D-IMP with 400 samples, and 5 data points per sweep. Left: result of sequential data assimilation with D-IMP for G12 and using Sint-2000 data. Right: Same but when assimilating synthetic data (Synt, see text and Fig. 8). (For interpretation of the references to colour in this figure legend, the reader is referred to the web version of this article.)

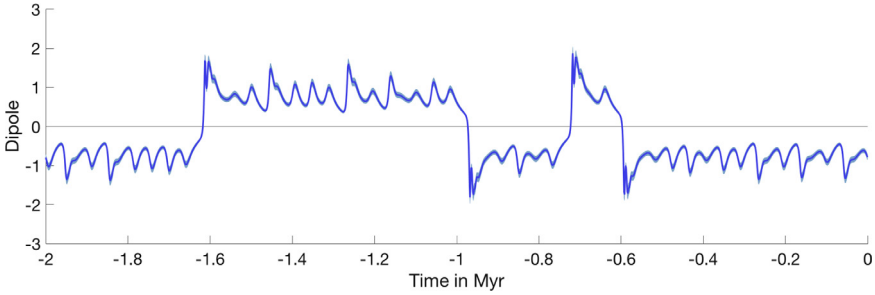


**Fig. 8.** "Synt" synthetic data computed from the G12 model. The blue line represents the mean and the light blue cloud represents the 95% confidence interval.

lead to a dipole sequence similar to that of the paleomagnetic data. We record the state every 1 kyr over a 2 Myr period, and add random errors that are distributed similarly to those of Sint-2000. Specifically, the errors are Gaussian and the standard deviation is chosen such that the mean of the relative paleointensity divided by the standard deviation of the errors is the same for Sint-2000 and the synthetic data. For the rest of this paper, we will refer to this synthetic data set as the "Synt" data set.

We observe discontinuities when assimilating this synthetic data, as illustrated in the top-right panel of Fig. 7. This is an important observation, since, by construction, the Synt data are intrinsically compatible with the G12 model. Our numerical experiment thus indicates that the discontinuities observed when assimilating the paleomagnetic data are more likely to be caused by the assimilation method, and in particular by the fact that only dipole data are assimilated. Specifically, we find that the errors after assimilation in the unobserved $Q$ and $V$ variables are larger than the errors in the observed dipole variable, namely 20% error in $Q$, 51% error in $V$.

In summary, we obtain small errors of about 3–8% in the dipole variables of all models, provided an appropriate data assimilation technique and a modest number of data points per sweep are used. The small errors suggest that G12 is indeed compatible with the paleomagnetic data. As before, compatible means that the data assimilation can keep the G12 dipole variable close to the data. This result is conditional on that no more than 5 kyr of data are assimilated, so that the limitations of G12, discussed in Section 2.3.1, do not come into play.

As pointed out by one of our reviewers, it is worth noting that data assimilation could also help discriminate models *not* being compatible with the paleomagnetic data. Based on our loose definition of compatibility, meaning errors being small, this would mean that errors of an incompatible model would become significantly larger, indicating that the model fails to capture even the basic dynamic behavior of the geomagnetic field, to the extent that no useful inference about this behavior could then be drawn. In this study, however, we do not investigate such ideas further and only focus on models that *are* compatible with the data.

## 4. Coarse predictions of dipole reversals

In the above section we showed that four low-dimensional models could be calibrated to paleomagnetic data as documented by Sint-2000 and PADM2M, in the sense that the average error in (4) is below 8%. This suggests that using these models and data assimilation may lead to simplified yet useful representations of the Earth's dipole, and that successful dipole reversal predictions may be based on calibrated model states. We investigate these issues carefully.

We wish to find out if low-dimensional models can reliably predict a time-window during which a reversal is likely to happen, without being precise about the timing of the reversal. The idea of such coarse prediction strategies is as follows. Given the model and data, a Monte Carlo based data assimilation computes a collection of model states that are compatible with the paleomagnetic data, in the sense that these states are samples from an appropriate posterior distribution. Each model state can be used to make a prediction by using it as an initial condition for a simulation over a specified time-window, called the "horizon". This leads to a cloud of trajectories that extend into the future, and these trajectories can be used to approximate the probability of a reversal within the horizon by computing the ratio of the number of trajectories that reverse to the total number of trajectories. For short horizons, the strategy "*predict that no reversal will occur within the horizon*" can be expected to be successful, and for extremely long horizons,

a reversal becomes likely. We consider 4 kyr and 8 kyr horizons, because they are relevant, since the horizon is comparable to the time the system needs to reverse, but shorter than a typical chron.

### 4.1. Hindcasting paleomagnetic data

We assess the success of coarse predictions by "hindcasting", i.e., by predicting the past. This technique is routinely used in numerical weather prediction and goes as follows. One assimilates data up to a specified time in the past and computes model states that are compatible with the data up to that time. One then evolves each state by the model, without assimilating more data. The trajectories one obtains in this way "predict" what happened in the past. Thus, hindcasting assesses how successful a prediction strategy is for predicting the future, by testing how successful it performs for past events.

For the hindcasts illustrated in Figs. 9–12, we assimilate Sint-2000 data, however similar results are obtained when PADM2M is used for assimilation. The assimilation is done by D-IMP and 200 samples, 5 data points per sweep for the G12 model, by S-EnKF with 400 samples for the G12 based SDE model, by S-IMP with 400 samples for B13, and by SIR with 400 samples for P09, for the reasons outlined in Section 3.

We start by considering scalar SDE models, a typical example of which is the P09 model. In Fig. 9 we show P09 based hindcasts for a 4 kyr horizon for the Brunhes–Matuyama (BM) reversal, which occurred between 777 and 776 kyr ago. Before the BM reversal, at $t = -781$ kyr, the system appears to be close to a branching point as a significant number of samples tend towards a reversal, while the majority of the samples indicate that the dipole variable will increase (top-left panel). Only a few of the 400 samples exhibit a reversal within the horizon, so that the predicted probability of a reversal is small (7%). At $t = -777$ kyr, as the system gets closer to the BM reversal, the majority of samples aligns and exhibits a decrease in the dipole amplitude (top-right panel), with 40% of the samples exhibiting a reversal within 4 kyr. Note that the geomagnetic dipole indeed reverses during this time window, i.e., the BM reversal is correctly predicted by 40% of the P09 trajectories. At $t = -773$ kyr, all trajectories exhibit a quick decrease of the dipole, however the decrease is quicker than the data (bottom-left panel). At $t = -769$ kyr, all P09 trajectories exhibit an overshoot (bottom-right panel). An overshoot is also observed in the data, however the overshoot happens later than predicted by P09.

We now turn to the case of the deterministic G12 model, and show, for comparison, G12 based hindcasts of the BM reversal (Fig. 10). We observe qualitatively similar results as when hindcasting by P09 (top row). However, the reversal is more accurately predicted by G12, since the majority of samples correctly predict that the dipole will decrease during the 4 kyr following $t = -781$ kyr. In fact, 94% of the trajectories reverse within 4 kyr of $t = -777$ kyr, which is the time window during which the reversal indeed occurred. The G12 hindcasts right after the reversal on the other hand appear unphysical, and increase after a brief decrease of the dipole (bottom row). We observe this unphysical behavior when hindcasting all reversals of the past 2 Myr.

It is important to check that the data assimilation can provide state estimates that are accurate enough so that predictions do not spread out so quickly that a reversal is always deemed likely within a 4–8 kyr time window. Put differently, we need to check that our data assimilation/forecasting system is not always calling for reversals. In this context we perform hindcasts during a time-period when no reversal occurred or was about to occur. Specifically, in Fig. 11, we show P09 based hindcasts during the Laschamp low-intensity event, which occurred approximately 40 kyr ago. We observe that none of the samples reverse within 4 kyr, which shows that the model correctly predicts that no reversal should have occurred. Note that in this context, a successful prediction is that *no* reversal occurs within the next 4–8 kyrs. Nonetheless, the system seems to be in a state of branching, because a large number of the samples predict that the signed relative paleointensity should keep increasing for the next 4 kyr, while at the same time, a large number of samples also predict that the signed relative paleointensity should decrease. In Fig. 12 we show G12 based

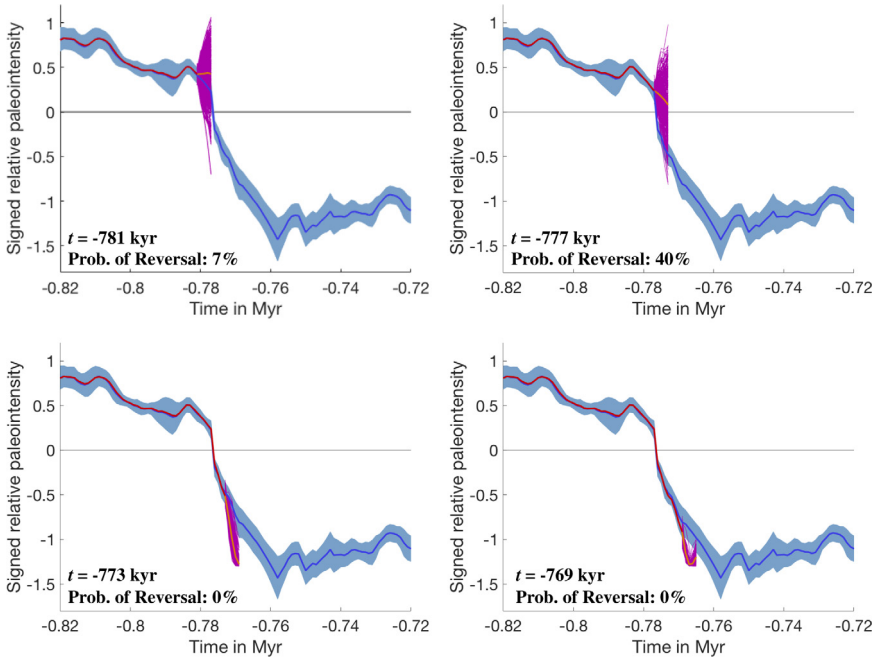


**Fig. 9.** Hindcasting the Brunhes–Matuyama reversal by P09. Blue: Sint-2000 data. Light blue cloud: 95% confidence interval. Red: data assimilation (Sint-2000 data, SIR, 400 samples). Purple: predictions over 4 kyr. Orange: average of predictions over 4 kyr. Top left to bottom right: hindcasting starts at $t = -781$ kyr, $t = -777$ kyr, $t = -773$ kyr, $t = -769$ kyr. (For interpretation of the references to colour in this figure legend, the reader is referred to the web version of this article.)

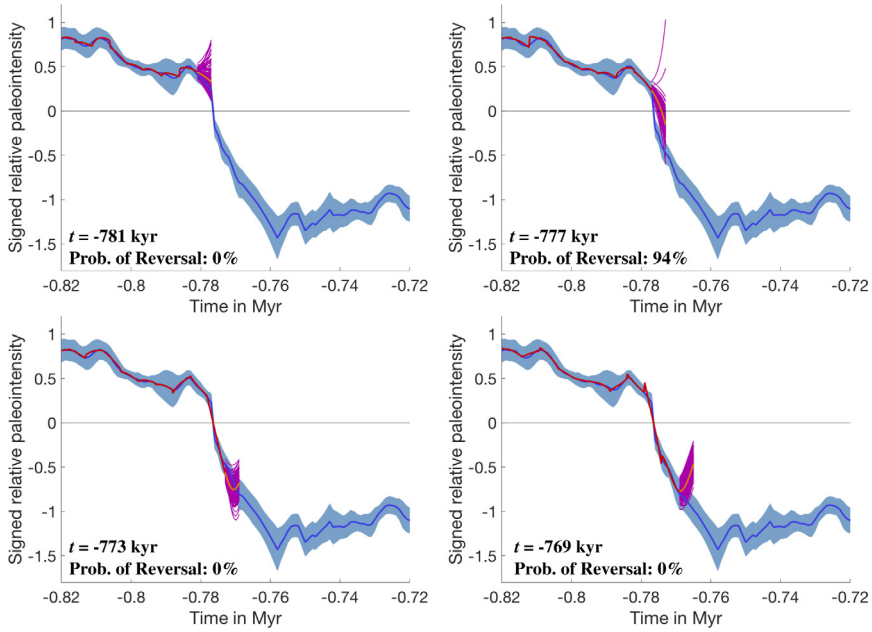


**Fig. 10.** Hindcasting the Brunhes–Matuyama reversal by G12. Blue: Sint-2000 data. Light blue cloud: 95% confidence interval. Red: data assimilation (Sint-2000 data, D-IMP, 200 samples, 5 observations per sweep). Purple: predictions over 4 kyr. Orange: average of predictions over 4 kyr. Top left to bottom right: hindcasting starts at $t = -781$ kyr, $t = -777$ kyr, $t = -773$ kyr, $t = -769$ kyr. (For interpretation of the references to colour in this figure legend, the reader is referred to the web version of this article.)

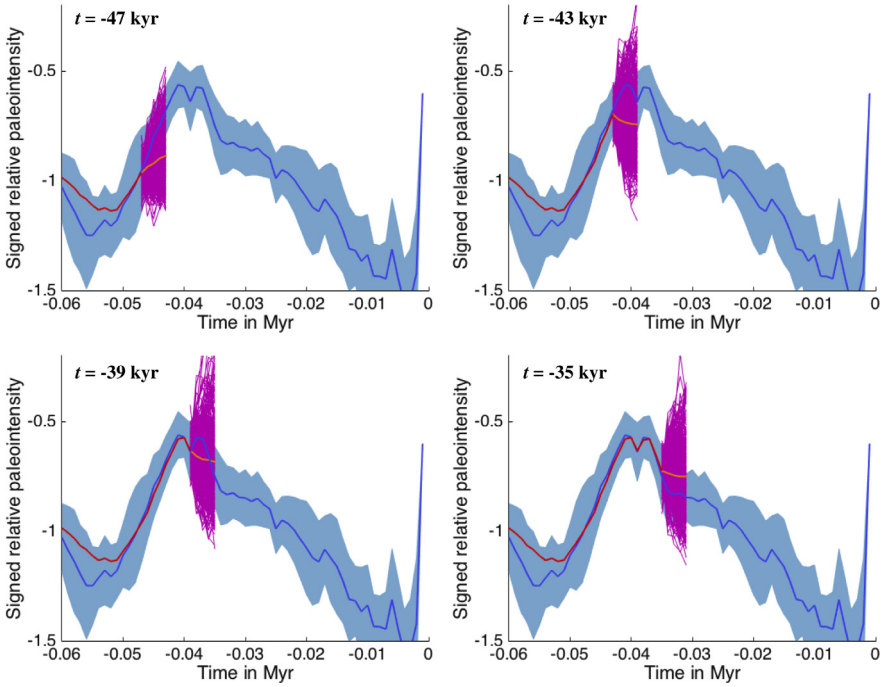


**Fig. 11.** Hindcasting by P09 during the Laschamp event. Blue: Sint-2000 data. Light blue cloud: 95% confidence interval. Red: data assimilation (Sint-2000 data, SIR, 400 samples). Purple: predictions. Orange: average of predictions. Top left to bottom right: hindcasting starts at $t = -47$ kyr, $t = -43$ kyr, $t = -39$ kyr, $t = -35$ kyr. (For interpretation of the references to colour in this figure legend, the reader is referred to the web version of this article.)

hindcasts of the same Laschamp event. The results we obtain are qualitatively similar, however immediately after the dipole field reaches its maximum value (at $t = -39$ kyr and $t = -35$ kyr), the G12 trajectories spread out more quickly than the samples of P09.

Indeed, we can perform hindcasts every 1000 years for all four models we consider, and compute the probability of a reversal to occur within a given horizon as a function of time. The results for all four low-dimensional models for a 4 kyr horizon when assimilating Sint-2000 data are shown in Fig. 13. We note that the probability graphs of all four models "peak" when the dipole indeed reverses. However, the B13 model assigns a low probability to the event "*a reversal occurs within 4 kyr*" at all times, even when a reversal is about to happen, with the maximum probability being about 30%. The graphs of the other three models, P09, G12 and G12 based SDE, look qualitatively similar to each other, and are somewhat noisier than the graph obtained with B13. We obtain

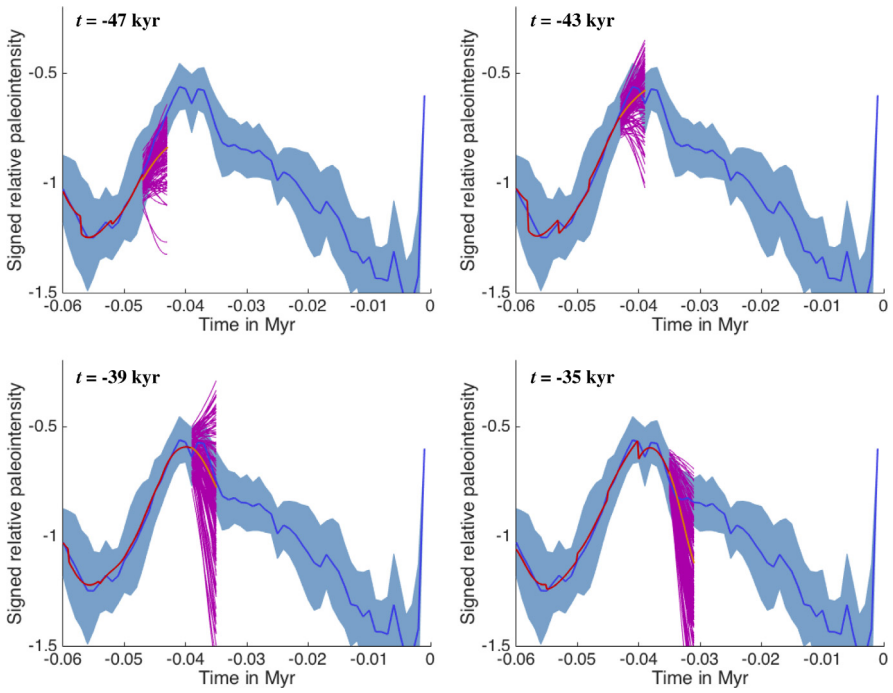


**Fig. 12.** Hindcasting by G12 during the Laschamp event. Solid blue: Sint-2000 data. Light blue cloud: 95% confidence interval. Red: data assimilation (Sint-2000 data, S-IMP, 200 samples). Purple: predictions over 4 kyr. Orange: average of predictions over 4 kyr. Top left to bottom right: hindcasting starts at $t = -47$ kyr, $t = -43$ kyr, $t = -39$ kyr, $t = -35$ kyr. (For interpretation of the references to colour in this figure legend, the reader is referred to the web version of this article.)

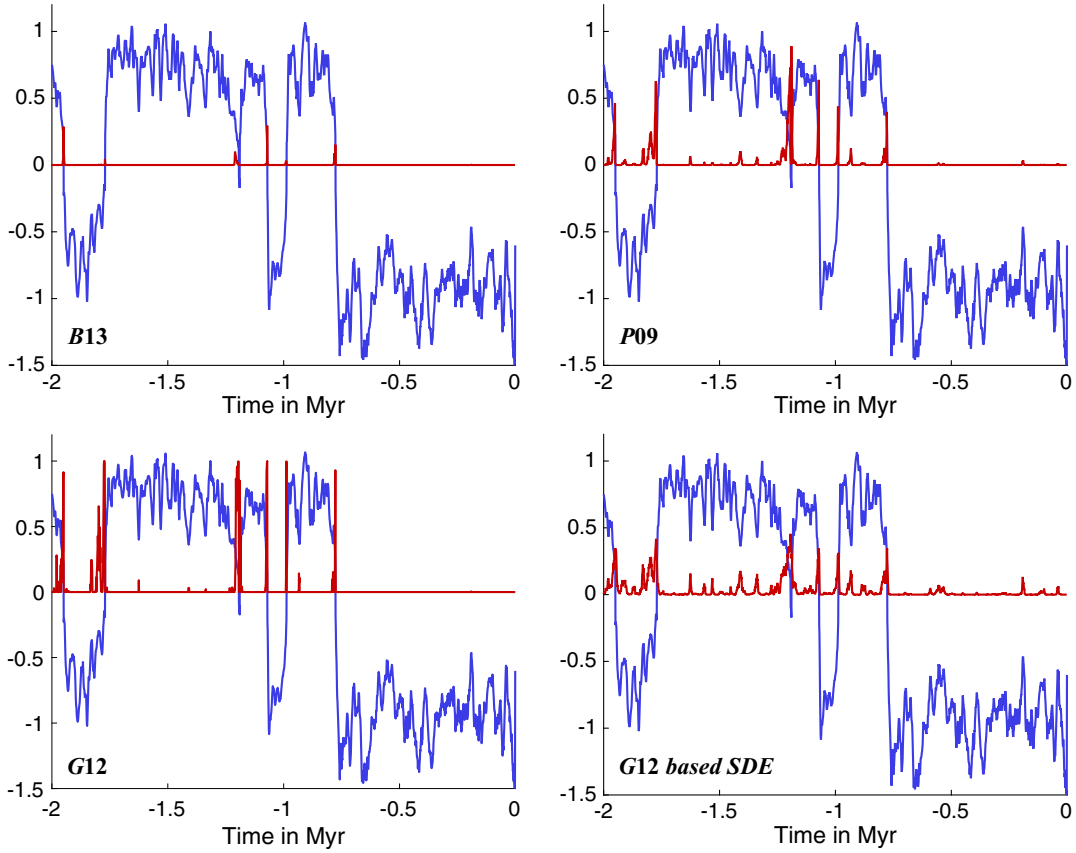


**Fig. 13.** Hindcasting by low-dimensional models. Shown is the predicted probability of a reversal to occur within 4 kyr as function of time (red) along with the Sint-2000 data (blue). Top-left to bottom-right: B13, P09, G12 and G12 based SDE models. (For interpretation of the references to colour in this figure legend, the reader is referred to the web version of this article.)

qualitatively and quantitatively similar results when PADM2M data are assimilated.

### 4.2. Inverse relative Brier score

The key question is: *which model leads to the most valuable predictions*? To answer this question, we need a quantitative assessment of the validity of predictions. A convenient tool for providing such an assessment is the Brier score, which uses hindcasts to measure the mean square error between computed probabilities and the actual outcome (Brier, 1950). This Brier score is defined by

$$b = \frac{1}{N}\sum_{j=1}^{N}(p_j - o_j)^2, \tag{5}$$

where $N$ is the number of hindcasts one makes, $p_j$ is the predicted probability of an event, and $o_j$ is a variable that is one if the event happens, and zero if it does not happen. For our purposes, the event is "*a reversal occurs within the horizon*", and $N = 2000$, i.e., we make hindcasts at each time we have a new datum between 2 Myr and 1 kyr ago.

We define a reference Brier score to assess how good coarse prediction strategies perform. This reference Brier score relies only on reversal statistics. Specifically, let $R$ be the number of times the event "*a reversal happened within the horizon*" happened, and let $N = 2000$ be the number of tries. The probability that a reversal happens, based solely on the reversal statistics of the past 2 Myr, is $p_{\text{stat}} = R/N$. For 4 kyr and 8 kyr horizons, $p_{\text{stat}} = 1.4\%$ and 2.6%, respectively. The reference Brier score can now be computed from Eq. (5) by setting $p_j = p_{\text{stat}}$ for $j = 1, \ldots, N$, with $p_{\text{stat}}$ as above. For the paleomagnetic data, the reference Brier scores are $b_{\text{ref}} = 0.013$ for a 4 kyr horizon, and $b_{\text{ref}} = 0.025$ for a 8 kyr horizon. We define the inverse relative Brier score (IRBS) as the ratio of the reference Brier score and the Brier score of the prediction strategy we wish to assess:

$$\text{IRBS} = b_{\text{ref}}/b_{\text{model}}. \tag{6}$$

IRBS values larger than 1 thus indicate that the prediction strategy is on average more reliable than a coin-toss, where the coin is biased by the probability $p_{\text{stat}}$. Note that such a coin does not at all behave like the "usual" head-and-tails coin with probability $p_{\text{stat}} = 50\%$.

Below we use IRBS to quantify how reliable a prediction strategy is. However, IRBS is far from being a perfect performance measure for dipole reversal predictions. The reason is that the event "*no reversal occurs within the horizon*" occurs more frequently than the event "*a reversal occurs within the horizon*". This means in particular that the strategy "*predict that no reversal will ever happen*" scores an IRBS slightly larger than one (specifically, 1.01 for a 4 kyr horizon, 1.02 for a 8 kyr horizon). On the other hand, this strategy is clearly not a good prediction strategy, since reversals are the relevant events here. One should thus keep in mind that prediction strategies that tend to assign a high probability to the event "*no reversal occurs within the horizon*" might be rendered successful by our IRBS measure, despite the fact they may grossly underestimate probabilities of reversals within time windows when a reversal actually occurred. Inadequacy of IRBS is amplified by limited amounts of data and these limitations are discussed further in Section 4.4 below.

### 4.3. IRBS comparison of data assimilation based prediction strategies

We compute IRBS for all four models, and when assimilating synthetic and paleomagnetic data. Experiments with synthetic data are essential here because these tests reveal whether or not the models are intrinsically predictable by the proposed strategy. Synthetic data are generated by the low-dimensional models using the state trajectories already shown in Fig. 2. Each data point has associated Gaussian errors whose variance is such that the mean of the relative paleointensity divided by the standard deviation of the errors is the same for Sint-2000 and for each of the four synthetic data sets. As before, we consider 4 kyr and 8 kyr horizons. Our results are summarized in Table 2.

We find that all four models yield IRBS larger than one when synthetic data are used and when the horizon is 4 kyr. This suggests that all models are intrinsically predictable over a 4 kyr horizon by our proposed strategy. We further obtain IRBS values larger than one for the B13, P09 and G12 based SDE models when considering predictions over a 8 kyr horizon. In contrast, the G12 model yields an IRBS less than one, which suggests that G12 is not intrinsically predictable over this longer horizon. The reason could be large errors in the unobserved variables $Q$ and $V$, which are proxies for un-modeled field and flow components. Large errors in these variables are indeed quickly amplified by G12's dynamics, leading to trajectories that spread out too quickly and too widely to be useful for predictions. In principle "more accurate data", or "more data", i.e., data of the quadrupole and velocity variables, could reduce these errors and make the G12 model predictable beyond the 4 kyr horizon, since its $e$-folding time is 40 kyr. In our experiments, however, we have to adjust the synthetic data to have roughly the same errors as the paleomagnetic data, and to acknowledge that data of other field or flow components are not available at this point. Thus, our synthetic data experiments suggest that, with the currently available paleomagnetic data, G12 can only predict dipole reversals within a 4 kyr horizon, and not for longer horizons.

We observe a significant drop in IRBS for all models and considered horizons when hindcasting paleomagnetic data. The reason is that model error can be expected to be significant, since all models are simplified representations of Earth's dipole dynamics. However, the results we obtain with either paleomagnetic data set, Sint-2000 or PADM2M, are very similar and predictions based on any of the four models still score IRBS larger than 1 for a 4 kyr horizon. P09, B13, and G12 based SDE also still score higher than 1 for the 8 kyr horizon. In contrast, G12 scores below 1 for a 8 kyr horizon, as in the above experiments with synthetic data.

Taken altogether, our assessment by IRBS is encouraging, as it suggests that all models have some predictive power even when paleomagnetic data are assimilated. In particular, we find that the P09 model scores the highest IRBS. However, IRBS can be high for inadequate reasons, and, therefore, can not represent sufficient evidence that a given prediction procedure is most reliable. We therefore assess the model-based predictions by an additional set of more stringent threshold-based prediction tests.

### 4.4. Threshold-based predictions

In threshold-based predictions one attaches a threshold to a parameter of a dynamic system and determines the probability of an event to occur by checking if the parameter is above or below the threshold. For example, one assigns probability one, i.e, predicting with certainty that the event will occur, if the parameter is above the threshold, and one assigns probability zero, i.e., predicting with certainty that the event will *not* occur, if the parameters is below its threshold. Alternatively, one can assign probability one if the parameter is below the threshold, and probability zero otherwise.

The success of threshold-based strategies depends on how the threshold is chosen and below we use an objective way to do this by splitting available data into two parts, "training data" and "verification data". We first "learn" the threshold from the training data

**Table 2**
IRBS for G12, stochastic G12, P09, and B13 models for 4 kyr and 8 kyr horizons and using synthetic data, Sint-2000, and PADM2M. IRBS values above 1 indicate that the data assimilation based strategy has more predictive capability than guessing based on reversal statistics.

| | Synthetic data | | Sint-2000 | | PADM2M | |
|---|---|---|---|---|---|---|
| Horizon | 4 kyr | 8 kyr | 4 kyr | 8 kyr | 4 kyr | 8 kyr |
| G12 | 3.49 | 0.47 | 1.21 | 0.35 | 1.13 | 0.25 |
| G12 based SDE | 1.40 | 1.43 | 1.28 | 1.23 | 1.19 | 1.10 |
| P09 | 1.89 | 2.05 | 1.51 | 1.63 | 1.50 | 1.93 |
| B13 | 1.42 | 1.41 | 1.01 | 1.15 | 1.06 | 1.08 |

as follows. We vary the threshold value, infer the corresponding (zero or one) threshold-based probabilities at each step, compute the corresponding IRBS score over training data, and finally find the threshold value that leads to the highest IRBS value. We then test the validity of the threshold by computing its IRBS score over the verification data.

*4.4.1. Intensity threshold-based predictions*

An example of a threshold-based prediction strategy for dipole reversals is "*a reversal will happen within the horizon if the intensity drops below a given threshold*". Note that this strategy relies on the intuitive fact that a reversal is more likely to occur in the near future if the paleomagnetic intensity is low, and that it does not make use of any dynamical considerations.

As explained above, we split the paleomagnetic data into two parts, "training data" and "verification data". The training data are the signed relative paleointensity from 2 Myr to 1.05 Myr ago, which includes five reversals, two of which occurred close to each other to define the Cobb mountain subchron, about 1.19 Myr ago. The verification data are the signed relative paleointensity from 1.05 Myr ago onwards, and include two reversals. We apply this strategy to Sint-2000 and PADM2M and consider a 4 kyr horizon. We show thresholds and associated IRBS values over the training data in the left panel of Fig. 14. We observe a well-defined extremum with IRBS well above one at an intensity threshold of 0.175 for both data sets (IRBS is 2.17 for Sint-2000 and 1.22 for PADM2M). This graph thus suggests that relying on an intensity threshold may indeed be a meaningful way of predicting reversals within a 4 kyr time-window. However, a posteriori using this optimal intensity threshold of 0.175 fails to predict several reversals, not only within the verification data, but also within the training data. Failure to correctly predict several reversals occurs independently of whether we use Sint-2000 or PADM2M (failures occurring when using Sint-2000 are illustrated in the bottom right panel of Fig. 15). The failure of this intensity threshold-based prediction strategy is interesting in two respects. Firstly, it shows that no intensity threshold-based strategy for either data set could pass our tests, which in turn suggests that the Earth's dynamo may not have an intensity threshold that can be used to infer that a reversal will inevitably occur (or at least we do not have data to back up such a strategy). Secondly, the result illustrates the fact that a prediction strategy scoring IRBS well above one over the available training data may still fail to provide relevant reversal predictions, even within the training data.

Testing the same intensity threshold-based prediction strategy when considering synthetic data produced by the four low-dimensional models also leads to instructive results. The data we use are those shown in Fig. 2, which we again split into training and verification data. In the case of the B13 or G12 based SDE models, we find that no threshold yields IRBS larger than one, whether considering the training or even the entire data sets. This suggests that the intensity of these models can become arbitrarily low without necessarily leading to a reversal. In the case of P09, the situation is slightly different and a maximum of 1.15 can be found for IRBS when considering a threshold 0.051. However, the threshold is rather low and the corresponding maximum IRBS value is poorly defined (the graph of IRBS vs. threshold is flat and does not exhibit a distinguished global maximum). Indeed, using the optimal threshold fails to lead to a successful prediction of all reversals within training and verification data which, as before, suggests that the intensity of the P09 model can also be very low without necessarily leading to a reversal. Experiments with synthetic data of the G12 model however result in successful predictions of all reversals by this intensity threshold-based prediction strategy. We find a clear IRBS maximum of 2.64 at a threshold 0.25 over the training data, which indeed is comparable to the threshold we obtained from Sint-2000 and PADM2M (see Fig. 14). In this respect, G12 appears to be more Earth-like than the stochastic models. On the

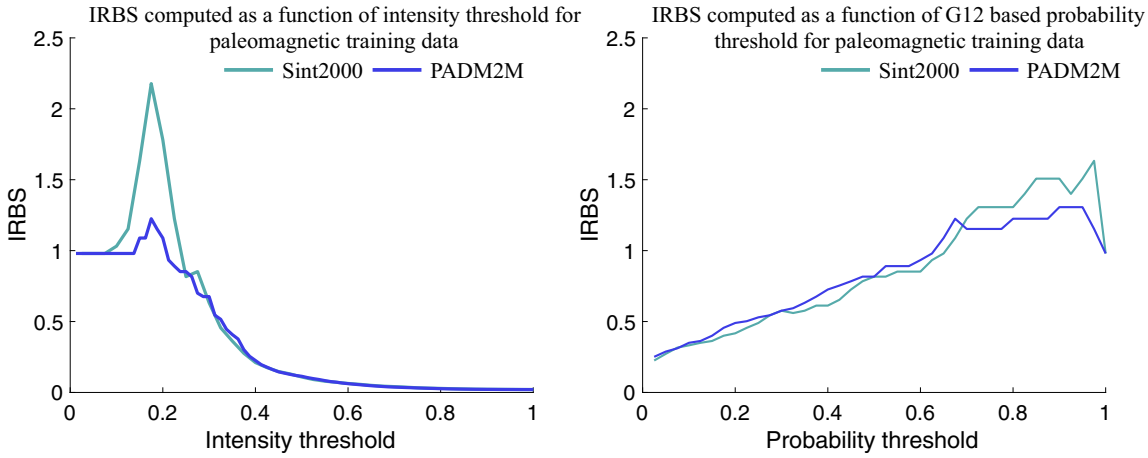


**Fig. 14.** Determining optimal intensity and probability thresholds. Shown is IRBS over paleomagnetic training data as a function of the intensity (left) and G12-based probability (right) thresholds.

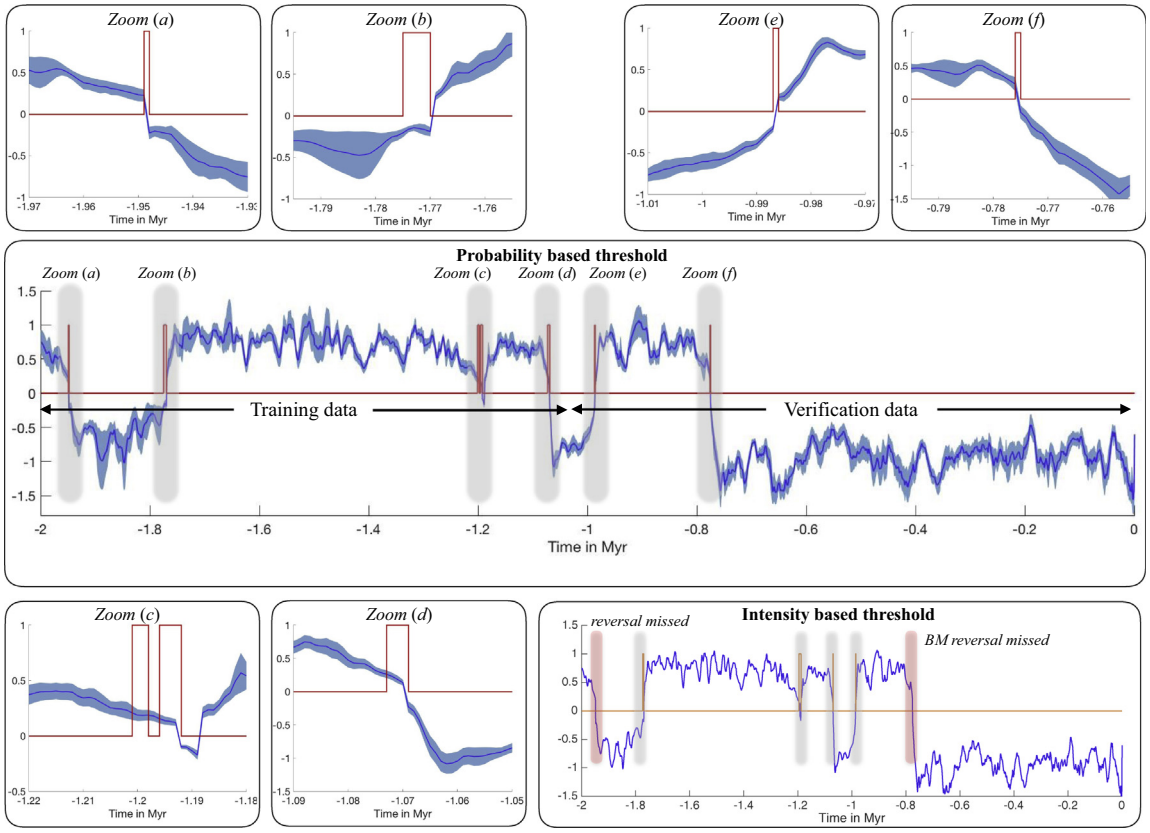


**Fig. 15.** Illustration of probability and intensity threshold-based reversal forecasts when considering Sint-2000 data. Center panel: hindcasting by probability threshold-based strategy when relying on the G12 model; blue – Sint-2000 data; light-blue cloud – 95% confidence intervals; red – coarse reversal prediction over 4 kyr horizon (indicator function is one if a reversal is predicted to happen, zero otherwise). Top row and bottom row, left two panels: magnified data and predictions. Bottom row, right panel: hindcasting by intensity-based threshold strategy; blue – Sint-2000 data; light-blue cloud – 95% confidence intervals; orange – reversal prediction over 4 kyr horizon. (For interpretation of the references to colour in this figure legend, the reader is referred to the web version of this article.)

other hand, it appears to be more predictable by intensity threshold-based strategies than the Earth's dynamo. This point will be further discussed below.

*4.4.2. Probability threshold-based predictions*

We now wish to test if low-dimensional models combined with data assimilation can provide a threshold criterium that is more reliable than the data-derived intensity threshold above. We thus modify the above intensity threshold-based strategy and predict that a reversal will occur with probability one within 4 kyr if the computed probability of an upcoming reversal exceeds a threshold, otherwise assign probability zero.

We first consider probabilities derived from the G12 model. The corresponding results are shown in the right panel of Fig. 14, where we show IRBS for the training data as a function of the probability threshold. We observe that the graph flattens for probability thresholds larger than 70%, and drops quickly for high probabilities larger than 98% for both paleomagnetic data sets. Specifically, the optimal threshold based on Sint-2000 is 97.5%, and for PADM2M threshold values between 90% and 95% are optimal, leading to IRBS values of 1.63 for Sint-2000, and 1.31 for PADM2M. When these optimal thresholds are used, we obtain an IRBS of 1.13 for the verification data of Sint-2000 and between 1.98 and 3.97 for the verification data of PADM2M (with optimal thresholds between 90% and 95%). In addition, both reversals within the verification data sets, whether Sint-2000 or the PADM2M, are correctly predicted (see Fig. 15).

While the G12 probability threshold-based strategy is somewhat successful, it also has weaknesses. For example, it leads to one false alert and fails to predict the reversal ending the Cobb mountain subchron (see zoom (c) in Fig. 15), when considering training data of Sint-2000. However, the false alert precedes a reversal by only 13 kyr and the reversal is correctly predicted by a later alert. In view of the much longer "typical" chron durations, such a false alert may be viewed as a "slightly too early" warning. Note that assessing the success of predictions by just relying on IRBS ignores the fact that predicting a reversal slightly too early is an error that is less severe than not predicting it at all.

Failing to predict the reversal ending the Cobb mountain subchron is of greater concern. This reversal occurred, according to the Sint-2000 data set, to within 4 kyr of the previous one. Failure to predict this reversal thus may result from inaccuracies within the Sint-2000 data. However, it may also suggest that the G12 model is incapable of producing two successive reversals within a few thousand years. This could be due to the fact that the deterministic G12 dynamics imposes a "minimum time" between reversals which may be significantly larger than what can be observed for this event.

Similar issues arise when using the PADM2M data set. In this case, no false alert occurs before the Cobb mountain subchron. However, a false alarm does occur shortly after (1kyr after the subchron), again indicating some incompatibility of the G12 model with this quick sequence of two reversals. The G12 model in combination with PADM2M and a probability threshold-based prediction strategy further fails to predict the upper Olduvai reversal (1.77 Myr ago) in the training data set. In this case, the alert is triggered only once the reversal actually occurred. We did not observe this behavior when using Sint-2000, which suggests that this behavior may indicate the limits of probability threshold-based strategies, especially in view of uncertainties in Sint-2000 or PADM2M.

We also apply the probability threshold-based prediction strategy to synthetic data of the G12 model, which yields positive results. We find an optimal probability-threshold of 87.5% and associated IRBS of 7.92 for the verification data, as well as fully successful predictions of all reversals. These tests indicate that some of the above issues could be caused by intrinsic limitations of the G12 model.

Finally, we also test probability threshold-based strategies for the three stochastic low-dimensional models P09, B13 and G12 based SDE. For the B13 and G12 based SDE models, no probability thresholds leading to IRBS significantly larger than one can be found, whether considering Sint-2000, PADM2M or synthetic data. This is reminiscent of the results we obtained by the intensity threshold-based strategy (see above). In other words, neither B13 nor the G12 based SDE model seem to provide successful probability threshold-based predictions, even when considering synthetic data produced by the models. The situation is again different for the P09 model. When using Sint-2000 data, the optimal threshold is 0.55, and the associated IRBS is 1.4 for the training data, and 0.99 for the verification data. Considering PADM2M data leads to a different, perhaps more encouraging result. We obtain an optimal threshold of 0.275 yielding an IRBS of 1.19 for the training data, and 2.47 for the verification data. However, when we consider synthetic data, we obtain a lower optimal probability threshold of 0.125, leading to an IRBS of 1.96 for the training data, and 0.5 for the verification data, failing to successfully predict reversals. The synthetic data experiment thus suggests that the probability-threshold based strategy is in fact not more applicable to P09 than to the other two stochastic models. These results are similar to what we found when we considered intensity threshold-based predictions for the P09 model (see above).

## 5. Summary and discussion

### 5.1. Summary of data assimilation

We considered three existing low-dimensional models, B13, P09 (both stochastic, Buffett et al., 2013; Pétrélis et al., 2009) and G12 (deterministic, Gissinger, 2012), and also proposed a new scalar stochastic model, the G12 based SDE, to describe the dynamics of the Earth's magnetic dipole over geological time scales (millions of years).

1. We find that the scaling of G12 model time is limited to match either a millennium scale, or a geological time scale. While this may be an intrinsic limitation of this model, it does not prevent the G12 model from being useful in the context of the present study, provided we use the millennium time scale.
2. We calibrated all four low-dimensional models to paleomagnetic data over the past 2 Myr by using "data assimilation". This was done by several numerical data assimilation techniques and by assimilation of two paleomagnetic data sets, Sint-2000 (Valet et al., 2005) and PADM2M (Ziegler et al., 2011).
3. We showed that all four low-dimensional models are compatible with both paleomagnetic data sets in the sense that average errors after data assimilation are no larger than 8%, provided a suitable numerical data assimilation method is used.

### 5.2. Summary of coarse reversal predictions

We further investigated the extent to which dipole reversals can be predicted to occur within time windows of 4 kyr and 8 kyr, without paying attention to the precise timing of the reversals within the time windows. The value of such coarse predictions was assessed by hindcasting experiments, i.e., "predicting past events", as is commonly done in numerical weather prediction. This led to the following findings.

1. Hindcasting experiments with data assimilation of synthetic data, i.e., data produced by the models, suggest that all four models (B13, P09, G12, G12 based SDE) are intrinsically predictable for time windows of 4 kyr, a necessary condition for the models to be useful as a prediction tool for Earth's dipole. The B13, P09 and G12 based SDE models are also intrinsically predictable over 8 kyr time windows.
2. When assimilating paleomagnetic data, as documented by Sint-2000 or PADM2M, and considering 4 kyr time windows, all four low-dimensional models perform "better", than making trivial reversal predictions based on reversal statistics of the past 2 Myr, as measured by higher inverse relative Brier scores (IRBS). Consistent with the results from synthetic data experiments, the P09, B13 and G12 based SDE models also perform well for 8 kyr windows. These findings suggests that low-dimensional models can indeed provide "useful" information and serve as a tool to understand and interpret paleomagnetic data.
3. Intensity threshold-based predictions are unsuccessful in the sense that we cannot obtain intensity thresholds from a "training data" set (of about 1 Myr, including five reversals), that lead to success when applied to a "verification data" set (of about 1 Myr, including two reversals). This purely data-based strategy fails to predict several reversals in both the training and verification data sets. This was found to be true for Sint-2000 and PADM2M data and suggests that, given the available data, paleomagnetic intensity can become low without necessarily being followed by a reversal within the next 4 kyr.
4. Similar intensity threshold-based prediction tests applied to synthetic data of the three stochastic models (B13, P09, G12 based SDE) suggest that the intensity of these models can be low without necessarily being followed by a reversal within the next 4 kyr. The deterministic G12 model on the other hand seems to have an intensity threshold, i.e., a reversal of the G12 dipole will necessarily occur if its intensity drops below a threshold.
5. Probability threshold-based predictions raise an "alert" for a reversal to occur within the next 4 kyr if the probability of a reversal inferred from low-dimensional models and data assimilation exceeds a given threshold. This strategy yields improved coarse predictions provided the G12 model is used. In contrast, stochastic models (B13, P09 and G12 based SDE) give unsatisfactory results. However, even when using the G12 model, probability threshold-based predictions have weaknesses. These are likely due to uncertainties of the Sint-2000 and PADM2M data we have not properly accounted for, as well as an inability of G12 to produce nearby reversals. The resulting "partial" failures, however, are not critical, and we conclude that a probability threshold-based strategy using the G12 model is more reliable than a purely data-based intensity threshold-based strategy.
6. Similar probability threshold-based prediction tests applied to synthetic data from the four low-dimensional models (B13, P09, G12 and G12 based SDE) further suggest that this strategy indeed fails for all stochastic models (B13, P09, or G12 based SDE), but not for the deterministic G12 model. The G12 model is the only model we consider for which a probability threshold can be found beyond which a reversal will necessarily occur.

All these results taken together provide interesting evidence that deterministic low-dimensional models such as G12 in combination with data assimilation can possibly provide a means for forecasting reversals within 4 kyr time windows. It should be

stressed, however, that the amount of paleomagnetic data we use for these tests is limited (only 2 Myr of data, documenting only seven reversals) and that errors affecting these data may not be properly accounted for. The above findings should thus be interpreted with caution.

### 5.3. Geophysical discussion and future work

Assessing whether or not reversals of the geomagnetic field can be forecasted is a challenging task which has already been addressed in the past. For example, several researchers have studied general characteristics of past reversals as well as the behavior of the field shortly before reversals (see, e.g., Valet and Fournier, 2016, for a recent review). Others have investigated the cause of the present fast decrease of the dipole field, which may be akin to processes that lead to reversals (see, e.g., Hulot et al., 2002; Finlay et al., 2016). Precursors of reversals were also identified from three-dimensional numerical dynamo simulations (see, e.g., Olson et al., 2009). However, identification of precursors within the details of the Earth's magnetic field before it reverses is difficult because of the particularly complex and varied ways the field can reverse, as is documented by paleomagnetic records and three-dimensional numerical simulations (see, e.g., Hulot et al., 2010a; Glatzmaier and Coe, 2015). As a matter of fact, no convincing precursor has yet been found in the way the modern field behaved in the recent past (see, e.g., Constable and Korte, 2006; Laj and Kissel, 2015). The search for precursors is further limited by the fact that details of the geomagnetic field are unlikely to be predictable beyond a century, as shown by investigations of three-dimensional numerical dynamo simulations (Hulot et al., 2010b; Lhuillier et al., 2011a). This limit of predictability is comparable to the time scale with which the detailed morphology of the geomagnetic field changes (Hulot and Le Mouël, 1994; Lhuillier et al., 2011b), but is much shorter than the time elapsed between reversals. This implies that the precise timing of a reversal (to within, say, a century) is likely to remain unknown until the reversal is just about to happen. However, this limit does not preclude that general macroscopic conditions for a reversal to occur within a wider time window could be found by examining the long-term dynamic behavior of the dipole field itself, which indeed displays a rich low-frequency temporal spectrum (Constable and Johnson, 2005). In this context, the horizon of predictability of the coarse behavior of the dipole field may be larger than that of the detailed behavior of the full field of the Earth's dynamo. This is the possibility we investigated here with the help of data of the past behavior of the dipole field, as documented by Sint-2000 and PADM2M, tentative low-dimensional models of the geodynamo, and data assimilation.

Two key results of geophysical relevance were obtained. One is that the available paleointensity data (Sint-2000 or PADM2M) do not seem to display any intensity threshold below which a reversal can be guaranteed to occur within the next 4 kyr. The second is that, in contrast, the very same data can be assimilated by the deterministic G12 model to make reliable predictions of reversals within 4 kyr time windows. It is important to emphasize that these results rely on the assumption that the signed relative paleointensity data provide a reliable source of information and accurately reflect the millennium dynamics of the Earth's magnetic field. Given our current understanding of the way sediments record this signal, these assumptions may not hold (see, e.g.,Valet and Fournier, 2016, for a discussion). In particular, relative timing of reversals with respect to the original paleointensity record is difficult to guarantee within a few kyr, and such paleointensity data are known to fail to record weak field intensities. In addition, the way sediment data average the original field intensity implies that paleointensity data contain some information about the near-future field intensity, at least up to 1 kyr, and possibly slightly beyond.

Another important limitation of the present study, which we already stressed, is the limited amount of reversals documented in the Sint-2000 and PADM2M data sets. This limitation, combined with the uncertainties affecting the data, may well impact IRBS, the exact values of the various thresholds we computed and, therefore, the significance of our results. However, the consistency of our findings with respect to the data, i.e., whether we use the Sint-2000 or PADM2M data sets, is encouraging.

Our study also revealed a number of interesting properties of the low-dimensional models we considered. While all four models succeed at assimilating the signed paleointensity data with comparable success (average errors after data assimilation are no larger than 8%), and appear to be intrinsically predictable in the coarse sense we defined, only predictions based on the deterministic G12 model pass the set of tests we devised. However, even the G12 model may not be considered as "satisfactory" for the purpose of coarse dipole predictions. For example, it fails to properly handle fast sequences of two successive reversals (such as those bounding the Cobb mountain subchron). It also produces sequences that display an intensity threshold that can be used to raise successful reversal alerts for G12, contrary to the paleointensity data as documented by Sint-2000 and PADM2M. Moreover, the G12 model is unable to properly reproduce the observed reversal frequency when scaled to the millennium time scale. Nonetheless, the successes of the G12 model in combination with the probability threshold-based prediction strategy indicates that these predictions may improve if "better" low-dimensional models could be obtained.

It is interesting in this respect to compare dipole data of the G12 model (not using any data assimilation) with the signed paleointensity data of Sint-2000 and PADM2M, and to investigate the causes of its success and failures. Comparing Figs. 1 and 2 (see also Fig. 8) makes it clear that the G12 dipole data is more regular than the paleomagnetic data. The fact that an intensity threshold can be found in the case of G12, and not in the case of the paleomagnetic data, can be traced back to this regularity. Local minima that do not lead to reversals in the G12 synthetic data are all of comparable magnitude. This is not the case in the paleomagnetic data. This is also not the case in the synthetic data produced by the three stochastic models B13, P09 and G12 based SDE, which were also found to lack reliable intensity thresholds (with the only possible exception of P09, which however displays a very low and poorly defined intensity threshold, as described in Section 4.4.1). In this respect, the dipole variable of the G12 model may be too regular when compared to Sint-2000 or PADM2M. Some regularity, however, has been found in the paleointensity data when the field approaches a reversal. In particular, it appears that this paleointensity tends to gradually decrease over a period of several 10 kyr before the reversal occurs (Valet et al., 2005). This medium-term dynamics is also found in dipole data produced by G12. Fig. 5 compares G12 dipole data with the paleointensity data of Sint-2000 during the Brunhes–Matuyama reversal. The figure shows that the synthetic data displays a gradual decrease at a rate comparable to the average rate seen in the paleointensity data, before dropping and leading to the reversal. No similar systematic feature is found in the synthetic data produced by the three unsuccessful stochastic models. This leads us to interpret that the success of G12 at correctly predicting reversals is resulting from the data assimilation scheme being capable of correctly picking up this trend in the paleointensity data, and thus setting G12 on its reversal path. This interpretation is also consistent with the fact that G12 partly failed at raising the proper alerts for the two reversals bounding the Cobb Mountain subchron, since the second reversal was not preceded by a medium-term intensity decrease. It is also consistent with the

fact that G12 succeeded at forecasting reversals despite its failure to properly account for the frequency of reversals. What really matters is the sequence of events preceding the reversal over the millennium timescale, which G12 was scaled to capture, and not the time elapsed since the last reversal.

The success of G12 at predicting past reversals may be a motivation to look for even better low-dimensional models, and the tests we derived provide means to assess any such model. The above discussion also highlights the fact that what matters most for a model to be a successful improvement upon G12 is that it better captures the dynamical path to a reversal. This was not the case of the three stochastic models we tested.

Possible routes to improvement of such stochastic models are to derive systems of SDEs (rather than scalar SDEs), as well as to include correlated noise terms (as in Buffett and Matsui, 2015). Improved deterministic models may be found as well. G12, in particular, could be improved by considering higher order terms or additional equations, e.g., more flow and field variables, while respecting the symmetries imposed by the background rotation. If the model dynamics become rich, one may need to account for the smoothing effect of sedimentation when considering the paleomagnetic data, but this could be handled, e.g., one could consider data assimilation with observation operators that model the sedimentation process. Finally, we note that $2\frac{1}{2}$-D dynamos (e.g., Sarson and Jones, 1999) could also be tested. With modern computers, data assimilation for such models is feasible, even over geological time scales. Any improvements, however, will depend on the validity of our underlying assumption that general conditions for reversals to occur are dictated by the average large-scale behavior of the dipole field, and not by the detailed morphology of the field, which plays a role only once the reversal is just about to happen. Although our study suggests this could be the case, this still needs to be confirmed.

For the time being, and based on what could be achieved using the G12 model and assimilating Sint-2000 and PADM2M data (up to 1 kyr ago), it is reassuring to see that no warning of any reversal is currently being raised for the next few millennia by our probability threshold-based approach. This result is consistent with the fact, already pointed out by several authors (e.g., Constable and Korte, 2006; Hulot et al., 2010a), that the current short-term fast decrease of the dipole field cannot alone be taken as evidence for an imminent reversal, even though it may possibly lead to temporarily low dipole field values (see, e.g., Laj and Kissel, 2015).

## Acknowledgements

We thank Jean-Pierre Valet of the Institut de Physique du Globe de Paris and Leah Ziegler of Oregon State University for assistance in using the SINT-2000 and PADM2M datasets. We thank Bruce Buffett, University of California at Berkeley, Francois Petrélis and Christophe Gissinger of Ecole Normale Supérieure, Paris, for interesting discussion and for providing their models for this study. We also thank Olivier Sirol of IPGP for valuable help with computing. We finally thank the reviewers for their very useful comments, which helped improve our manuscript and provided us with many suggestions for future additional work.

This material is based upon work supported by the U.S. Department of Energy, Office of Science, Office of Advanced Scientific Computing Research, Applied Mathematics Program under contract DE-AC02005CH11231, by the National Science Foundation under grants DMS-1419044 and DMS-1619630, by IPGP's Visiting Program, CNRS PNP program, and by the Alfred P. Sloan Foundation through a Sloan Research Fellowship awarded to MM. This is IPGP contribution n° 3787.

## Appendix A. Average *e*-folding time of the G12 model

The *e*-folding time describes the time required for errors to grow by a factor *e* and, thus, provides a measure of how far into the future one can rely on G12 based predictions. For example, once small errors are amplified to be macroscopic, model based predictions are dominated by error. One can thus expect that G12 based predictions can be reliable at most for time-horizons comparable to the model's *e*-folding time. Similarly, propagating information from data backwards in time over several *e*-folding times will be numerically difficult.

We estimate the *e*-folding time of G12 as follows. First we determine an initial condition on the attractor by simulating G12 for 10 Myr from an arbitrary point in state space; the last state of this simulation is likely to be on the attractor, or at least close to it. We pick this state to be the initial condition, and perturb it by a Gaussian with mean zero and covariance $10^{-10}$ times the identity matrix $I$. We generate 100 random perturbations and, for each of these, compute the error as a function of time for the next 4 Myr. The error is the Euclidean norm of the difference of the reference solution and the perturbation. The average error over the 100 samples can be used to estimate the *e*-folding time by a log-linear least squares fit.

Our estimate of the *e*-folding time depends on where we start the simulations. To account for this variation, we average the *e*-folding time over the attractor, and repeat the above procedure with the last state of the reference trajectory serving as the initial condition for the next calculation. We do this 500 times to obtain 500 samples of the *e*-folding time at various locations of 2000 Myr on the attractor. The results are shown in Fig. 16. We then compute the average *e*-folding time over these 500 samples and this average *e*-folding time is 40 kyr.

## Appendix B. Overview of the data assimilation methods we used

The goal in data assimilation is to combine a mathematical model with information from sparse and noisy data. This is done via Bayesian statistics and conditional probability. Here we briefly review data assimilation and summarize the numerical techniques we use. More detailed reviews of data assimilation in geophysics can be found in Bocquet et al. (2010); van Leeuwen (2009);

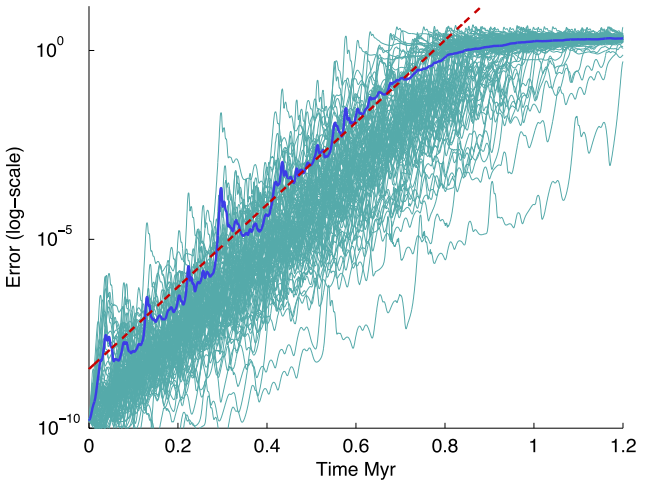


**Fig. 16.** Error as a function of time. The thin turquoise lines are 500 samples of the average error, each corresponding to perturbations of a given initial condition. The thick blue line is the average over these 500 samples. The red line is a log-linear fit. (For interpretation of the references to colour in this figure legend, the reader is referred to the web version of this article.)

Fournier et al. (2010); Blayo et al. (2014). For earlier applications of data assimilation in geomagnetism, see Fournier et al. (2007); Sun et al. (2007); Fournier et al. (2011); Aubert and Fournier (2011); Morzfeld and Chorin (2012).

### B.1. Data assimilation with deterministic models

Suppose you have a mathematical model in the form of an ordinary differential equation (ODE) (e.g., the G12 model). After discretization, e.g., with a Runge–Kutta scheme, the discrete model can be written as

$$x^n = \mathscr{M}_n(x^0),$$

where $x^n$ is an $m$-dimensional column vector approximating the solution of the underlying ODE at some time $t_n$, and where $x^0$ is the state at time 0, i.e., the initial condition of the ODE. For example, for the G12 model, $x^n = [D(t=t_n), Q(t=t_n), V(t=t_n)]^T$, in which superscript $T$ means transpose. Suppose you have collected data at time $t_n$. Then the state at time 0 and the data at time $t_n$ are connected by

$$z^n = h(\mathscr{M}_{t_n}(x^0)) + v, \tag{7}$$

where $z^n$ is a $k$-dimensional vector containing the data, $h(x)$ is a given vector function, and $v$ is a random variable that accounts for the imperfection of the mathematical model and measurement. We will assume throughout that $v$ is Gaussian with mean zero and with a given $k \times k$ symmetric and positive definite covariance matrix $R$. The above Eq. (7) defines the *likelihood* $p(z^n \mid x^0)$, which describes the probability of the data given the initial condition $x^0$. Here and below, a vertical bar denotes conditioning of random variables.

We assume that the state at time 0 is not completely known, but described by a *prior* probability density $p(x^0)$, which may be a Gaussian with a given mean and variance. The prior is chosen before the data are collected. The prior and the likelihood jointly define a *posterior* probability

$$p(x^0 \mid z^n) \propto p(x^0)p(z^n \mid x^0), \tag{8}$$

which contains all the information we have given the model and the data. For example, one can use the posterior distribution to compute the conditional mean, which is the minimum mean square error estimate of the state (see, e.g., Chorin and Hald, 2013).

In data assimilation we find the posterior distribution by various numerical techniques. In the case of variational data assimilation (Bennet et al., 1993; Talagrand and Courtier, 1987), one finds the most likely state, given the data, by maximizing the posterior probability. Alternatively, Monte Carlo sampling can be used to obtain an empirical estimate of the posterior (Kalos and Whitlock, 1986; Atkins et al., 2013; Chorin and Hald, 2013). This empirical estimate consists of a set of weighted samples $\{w_j, X_j^0\}$, $j = 1, \ldots, M$, such that averages over the samples converge to expected values with respect to the posterior. The Monte Carlo approach also makes it possible to incorporate errors (in model and data) into our estimation. For example, the accuracy of a state estimate can be known by computing the standard deviations of the samples. In addition, each sample can be used to produce an individual forecast, so that the Monte Carlo approach can lead to reliable forecasting, in which the uncertainty in the estimate is accounted for. In practice, many variants of these methods can be used. Below, we summarize the techniques we relied on.

#### B.1.1. Implicit sampling

Implicit sampling is a technique that combines ideas from variational data assimilation with Monte Carlo sampling. Details and different implementations of implicit sampling can be found in Chorin and Tu (2009); Chorin et al. (2010); Morzfeld et al. (2012); Atkins et al. (2013); Morzfeld and Chorin (2012). Here, we only briefly describe the principle of the algorithm.

The samples are generated by a data-informed probability. To find this probability, define

$$F(x^0) = -\log p(x^0 \mid z^n) = -\log p(x^0) - \log p(z^n \mid x^0).$$

Specifically, for a Gaussian prior with mean $\mu_0$ and covariance $\Sigma_0$, and for $v \sim \mathscr{N}(0, R)$, we find that

$$F(x^0) = \frac{1}{2}(x^0 - \mu_0)^T \Sigma_0^{-1}(x^0 - \mu_0) + \frac{1}{2}\left(h(\mathscr{M}_{t_n}(x^0)) - z^n\right)^T R^{-1}\left(h(\mathscr{M}_{t_n}(x^0)) - z^n\right).$$

Let

$$\mu = \arg\ \min F(x^0), \quad \phi = \min F(x^0),$$

be the minimizer and minimum of $F$, respectively, and let $H$ be the Hessian of $F$ at the minimum (i.e., the $m \times m$ symmetric positive definite matrix whose elements are the second derivatives of $F$). In implicit sampling, the samples are generated by the Gaussian

$$X_j^0 \sim \mathscr{N}(\mu, H^{-1}),$$

and the weights are

$$w_j \propto \exp\left(F_0(X_j^0) - F(X_j^0)\right),$$

where

$$F_0(x^0) = \phi + \frac{1}{2}(x^0 - \mu)^T H(x^0 - \mu),$$

is the Taylor approximation of $F$ to second order. In summary, the implicit sampling algorithm is:

1. find the minimum of $F$ (similar to variational data assimilation);
2. generate samples using the Gaussian $\mathscr{N}(\mu, H^{-1})$;
3. compute the weights $w_j = \exp(F_0(X_j^0) - F(X_j^0))$ for each sample.

The result is a set of weighted samples which approximate the posterior probability (8).

#### B.1.2. Sequential data assimilation

The data assimilation approach can be extended to data assimilation problems with more than one datum. Suppose there are $n$ data points $z^1, \ldots, z^i, \ldots, z^n$, collected at times $t_1, \ldots, t_i, \ldots, t_n$. Then the posterior probability (8) becomes

$$p(x^0 \mid z^{1:n}) \propto p(x^0)p(z^1 \mid x^0) \cdots p(z^i \mid x^0) \cdots p(z^n \mid x^0),$$

where we use the notation $z^{1:n}$ for the set of vectors $\{z^1, \ldots, z^i, \ldots, z^n\}$, and the "likelihood" of each datum, $p(z^i \mid x^0)$, is specified by an equation of the form (7). For example, if the noise at time $t_i$ is Gaussian with mean zero and variance $R_i$, then $p(z^i \mid x^0) = \mathscr{N}(h(\mathscr{M}_{t_i}(x^0)), R_i)$.

One can modify this approach to work sequentially as follows. Suppose $n$ data are available at times $t_1, \ldots, t_n$. We first pick the first $l < n$ of these data and compute the posterior

$$p_l(x^0 \mid z^{1:l}) \propto p(x^0)p(z^1 \mid x^0)\, p(z^2 \mid x^0) \cdots p(z^l \mid x^0).$$

This can be done using the same implicit sampling technique as before. We however next remove the weights by a resampling step, during which we delete samples with a small weight, and duplicate samples with a large weight (see, e.g., Doucet et al., 2001 for resampling algorithms). The result is a set of $M$ unweighted sam-

ples of this first posterior at time 0. The samples are informed by the first $l$ data points. We then propagate these samples forward to time $t_l$ by the model:

$$X_j^l = \mathscr{M}_{t_l}(X_j^0), \quad j = 1, \ldots, M$$

and compute the mean and variance of these samples to construct a Gaussian $p(x^l)$ that describes the state at time $t_l$.

This Gaussian $p(x^l)$ is next used as a *prior* for the state at time $t_l$, to proceed with the assimilation of the next $l$ data points. We simply update this prior to the posterior

$$p_l(x^l \mid z^{l+1:2l}) \propto p(x^l)p(z^{l+1} \mid x^l)\, p(z^{l+1} \mid x^l) \cdots p(z^{2l} \mid x^l)$$

and use the same implicit sampling and resampling steps as above to draw samples $X_j^l$ from this posterior. These unweighted samples then represent the state at time $t_l$, given the data $z^{1:2l}$. At this point, the information from the first $l$ data points was used in the prior $p(x^l)$, and the next $l$ data points were used to update this prior to the posterior. These samples can then again be forwarded, now to time $t_{2l}$, to produce a Gaussian *prior* $p(x^{2l})$ for the state at time $t_{2l}$, which can again be used to proceed with the assimilation of the next $l$ data points. This process can be repeated, using $l$ data per sweep, until all data are assimilated. We will refer to this method as the sequential data assimilation with implicit sampling method for deterministic models (D-IMP, for short).

*B.1.3. The ensemble Kalman filter*

The ensemble Kalman filter (EnKF) is a different numerical data assimilation technique, which computes a Gaussian approximation of the posterior probability $p(x^n \mid z^{1:n})$ at any time $t_n$ when data are collected (Evensen, 2006). The EnKF is recursive algorithm and works as follows. First recall that $z^n$ is assumed to satisfy (7), however we assume for EnKF that the "observation operator" $h$ is linear, i.e., $h(x) = Hx$, where $H$ is a matrix. Next, suppose you have $M$ samples of the posterior at time $n-1$, $X_j^{n-1} \sim p(x^{n-1} \mid z^{1:n-1})$. Then, for each sample, compute

$$\widehat{X}_j^n = \mathscr{M}_{t_n}(X_j^{n-1}),$$

and let $C$ be the sample covariance matrix. With this covariance, define the Kalman gain

$$K = CH^T(HCH^T + R)^{-1},$$

where $R$ is the covariance matrix of the random variable $v$. The Kalman gain is used to compute the "analysis ensemble":

$$X_j^n = \widehat{X}_j^n + K\left(\hat{z}_j^n - H\widehat{X}_j^n\right),$$

where $\hat{z}_j^n$ is a "perturbed observation" obtained from $\hat{z}_j^n = z^n + V_j, V_j$ being a sample of $v$.

The EnKF then provides a state estimate at each time $t_n$ when the data are collected. Note that EnKF produces a Gaussian approximation of the posterior. This can lead to large errors in nonlinear problems, where this approximation is not valid. We will refer to this method as the EnKF method for deterministic models (D-EnKF, for short).

*B.2. Data assimilation with stochastic models*

Data assimilation can also be applied to stochastic models (such as the B13 and P09 models considered in this study). It is typical in data assimilation to consider only discrete-time models and we follow suit. A time discretization of an SDE (1) can be written as

$$x^n = \hat{f}(x^{n-1}) + \hat{g}(x^{n-1})\Delta W,$$

where $\hat{f}$ and $\hat{g}$ depend on the discretization we use, and where $\Delta W$ is a Gaussian with mean zero and whose variance is equal to the time step size $\delta t$ (see, e.g., Kloeden and Platen, 1999). Data are collected at discrete times:

$$z^n = h(x^n) + v^n,$$

where $v^n$ are independent Gaussian random variables with mean zero and variance $R^n$.

The posterior of interest is $p(x^{0:n} \mid z^{1:n})$ and a sequential approach, based on the recursion,

$$p(x^{0:n} \mid z^{1:n}) \propto p(x^{0:n-1} \mid z^{1:n-1})\, p(x^n \mid x^{n-1})p(z^n \mid x^n), \tag{9}$$

is often used. Here, we use a sequential Monte Carlo approach (Doucet et al., 2001), and apply Monte Carlo sampling (recall above) at each step of the recursion to the "update" of the posterior, $p(x^n \mid x^{n-1})p(z^n \mid x^n)$. The "prior",

$$p(x^n \mid x^{n-1}) = \mathscr{N}\left(\hat{f}(x^{n-1}), \delta t \hat{g}(x^{n-1})\hat{g}(x^{n-1})^T\right)$$

is then defined by the discretized stochastic model, while the "likelihood",

$$p(z^n \mid x^n) = \mathscr{N}(h(x^n), R^n),$$

is defined by the data. The product of the prior and likelihood thus defines the posterior update we sample at each step. Again we use implicit sampling at each step to sample the posterior update $p(x^n \mid x^{n-1})p(z^n \mid x^n)$ (for the assimilations we perform in the manuscript, implicit sampling is in fact the optimal sampling strategy, see Morzfeld et al. (2012)). Over time, one obtains, recursively, an empirical estimate of the posterior (9). We will refer to this method as the sequential data assimilation with implicit sampling method for stochastic models (S-IMP, for short).

In addition, we will also use sequential importance sampling with resampling (SIR) (Doucet et al., 2001). In this method, one picks the prior as the importance function for the posterior update at each step. The weights are proportional to the likelihood. In short, the algorithm updates the posterior at time $n-1$, represented by $M$ samples to time $n$ as follows: (*i*) for each sample, simulate the model to time $n$; and (*ii*) compute the weight from the likelihood $p(z^n \mid x^n)$; repeat for all $M$ samples. This method is easy to implement, however becomes inefficient if the dimension of the problem increases. We will refer to this method as the SIR method.

Finally, we will also use EnKF for data assimilation with the stochastic models. Indeed, EnKF can readily be extended to stochastic models by generating the "forecast ensemble" (see above) with the stochastic model. The remaining formulas of EnKF for stochastic models are then as defined above. We will refer to this method as the EnKF method for stochastic models (S-EnKF, for short).

## References


Amit, H., Leonhardt, R., Wicht, J., 2010. Polarity reversals from paleomagnetic observations and numerical dynamo simulations. Space Sci. Rev. 155 (1–4), 293–335.

Atkins, E., Morzfeld, M., Chorin, A., 2013. Implicit particle methods and their connection with variational data assimilation. Mon. Weather Rev. 141, 1786–1803.

Aubert, J., Fournier, A., 2011. Inferring internal properties of Earth's core dynamics and their evolution from surface observations and a numerical geodynamo model. Nonlinear Processes Geophys. 18, 657–674.

Bennet, A., Leslie, L., Hagelberg, C., Powers, P., 1993. A cyclone prediction using a barotropic model initialized by a general inverse method. Mon. Weather Rev. 121, 1714–1728.

Blayo, E., Bocquet, M., Cosme, E., Cugliandolo, L.F., 2014. Advanced Data Assimilation for Geosciences. Oxford University Press.

Bocquet, M., Pires, C., Wu, L., 2010. Beyond Gaussian statistical modeling in geophysical data assimilation. Mon. Weather Rev. 138, 2997–3023.

Brendel, K., Kuipers, J., Barkema, G., Hoyng, P., 2007. An analysis of the fluctuations of the geomagnetic dipole. Phys. Earth Planet. Inter. 162, 249–255.
Brier, G., 1950. Verification of forecasts expressed in terms of probability. Mon. Weather Rev. 78 (1), 1–3.
Buffett, B., 2015. Dipole fluctuations and the duration of geomagnetic polarity transitions. Geophys. Res. Lett. 42, 7444–7451.
Buffett, B., Matsui, H., 2015. A power spectrum for the geomagnetic dipole moment. Earth Planet. Sci. Lett. 411, 20–26.
Buffett, B., Ziegler, L., Constable, C., 2013. A stochastic model for paleomagnetic field variations. Geophys. J. Int. 195 (1), 86–97.
Buffett, B.A., King, E.M., Matsui, H., 2014. A physical interpretation of stochastic models for fluctuations in the earth's dipole field. Geophys. J. Int. 198 (1), 597–608.
Cande, S., Kent, D., 1995. Revised calibration of the geomagnetic polarity timescale for the late cretaceous and cenozoic. J. Geophys. Res. Solid Earth 100, 6093–6095.
Chorin, A., Hald, O., 2013. Stochastic Tools in Mathematics and Science. Springer.
Chorin, A., Tu, X., 2009. Implicit sampling for particle filters. Proc. Nat. Acad. Sci. 106 (41), 17249–17254.
Chorin, A., Morzfeld, M., Tu, X., 2010. Implicit particle filters for data assimilation. Communications in Applied Mathematics and Computational Science 5 (2), 221–240.
Constable, C., Johnson, C., 2005. A paleomagnetic power spectrum. Phys. Earth Planetary Inter. 153, 61–73.
Constable, C., Korte, M., 2006. Is Earth's magnetic field reversing? Earth Planet. Sci. Lett. 246, 1–16.
Doucet, A., de Freitas, N., Gordon, N., 2001. Sequential Monte Carlo Methods in Practice. Springer.
Evensen, G., 2006. Data Assimilation: The Ensemble Kalman Filter. Springer.
Feingold, G., Koren, I., 2013. A model of coupled oscillators applied to the aerosol-cloud-precipitation system. Nonlinear Processes Geophys. 20, 1011–1021.
Finlay, C.C., Aubert, J., Gillet, N., 2016. Gyre-driven decay of the earth's magnetic dipole. Nat. Commun. 7, 10422.
Fournier, A., Eymin, C., Alboussière, T., 2007. A case for variational geomagnetic data assimilation: insights from a one-dimensional, nonlinear, and sparsely observed MHD system. Nonlinear Processes Geophys. 14, 163–180.
Fournier, A., Hulot, G., Jault, D., Kuang, W., Tangborn, W., Gillet, N., Canet, E., Aubert, J., Lhuillier, F., 2010. An introduction to data assimilation and predictability in geomagnetism. Space Sci. Rev. 155, 247–291.
Fournier, A., Aubert, J., Thébault, E., 2011. Inference on core surface flow from observations and 3-D dynamo modelling. Geophys. J. Int. 186, 118–136.
Gallet, Y., Hulot, G., 1997. Stationary and nonstationary behavior within the geomagnetic polarity time scale. Geophys. Res. Lett. 24 (15), 1875–1878.
Gissinger, C., 2012. A new deterministic model for chaotic reversals. Eur. Phys. J. B 85, 137.
Gissinger, C., Dormy, E., Fauve, S., 2010. Morphology of field reversals in turbulent dynamos. EPL (Europhys. Lett.) 90 (4), 49001.
Glatzmaier, G., Coe, R., 2015. Magnetic polarity reversals in the core. In: Core Dynamics. . second ed.. In: Olson, P., Schubert, G. (Eds.), . Treatise on Geophysics second ed., vol. 8 Elsevier, Amsterdam, pp. 279–295. chap. 9.
Glatzmaier, G.A., Roberts, P.H., 1995. A three-dimensional convective dynamo solution with rotating and finitely conducting inner core and mantle. Phys. Earth Planet. Inter. 91, 63–75.
Gubbins, D., Zhang, K.K., 1993. Symmetry properties of the dynamo equations for paleomagnetism and geomagnetism. Phys. Earth Planet. Inter. 75 (4), 225–241.
Hoyng, P., Ossendrijver, M., Schmitt, D., 2001. The geodynamo as a bistable oscillator. Geophys. Astrophys. Fluid Dyn. 94, 263–314.
Hulot, G., Le Mouël, J.-L., 1994. A statistical approach to the Earth's main magnetic field. Phys. Earth Planet. Inter. 82, 167–183.
Hulot, G., Eymin, C., Langlais, B., Mandea, M., Olsen, N., 2002. Small-scale structure of the Geodynamo inferred from Oersted and Magsat satellite data. Nature 416, 620–623.
Hulot, G., Finlay, C.C., Constable, C.G., Olsen, N., Mandea, M., 2010a. The magnetic field of planet Earth. Space Sci. Rev. 152, 159–222.
Hulot, G., Lhuillier, F., Aubert, J., 2010b. Earth's dynamo limit of predictability. Geophys. Res. Lett. 37, L06305.
Kalos, M., Whitlock, P., 1986. Monte Carlo Methods. John Wiley and Sons. vol. 1.
Kloeden, P.E., Platen, E., 1999. Numerical Solution of Stochastic Differential Equations. Springer.
Koren, I., Feingold, G., 2011. Aerosol-cloud-precipitation system as a predator-pray problem. Proc. Nat. Acad. Sci. 108 (30), 12227–12232.
Kuipers, J., Hoyng, P., Wicht, J., Barkema, G., 2009. Analysis of the variability of the axial dipole moment of a numerical dynamo model. Phys. Earth Planet. Inter. 173, 228–232.
Laj, C., Kissel, C., 2015. An impending geomagnetic transition? Hints from the past. Front. Earth Sci. 3, 61.
Lhuillier, F., Aubert, J., Hulot, G., 2011a. Earth's dynamo limit of predictability controlled by magnetic dissipation. Geophys. J. Int. 186, 492–508.
Lhuillier, F., Fournier, A., Hulot, G., Aubert, J., 2011b. The geomagnetic secular-variation timescale in observations and numerical dynamo models. Geophys. Res. Lett. 38, L09306.
Lhuillier, F., Hulot, G., Gallet, Y., 2013. Statistical properties of reversals and chrons in numerical dynamos and implications for the geodynamo. Phys. Earth Planet. Inter. 220, 19–36.
Lowrie, W., Kent, D., 2004. Geomagnetic polarity time scale and reversal frequency regimes. Timescales of the Paleomagnetic Field 145, 117–129.
McFadden, P., Merrill, R., McElhinny, M., Lee, S., 1991. Reversals of the Earth's magnetic field and temporal variations of the dynamo families. J. Geophys. Res. Solid Earth 93, 3923–3933.
Meduri, D., Wicht, J., 2016. A simple stochastic model for dipole moment fluctuations in numerical dynamo simulations. Front. Earth Sci. 4, 38.
Morzfeld, M., Chorin, A., 2012. Implicit particle filtering for models with partial noise, and an application to geomagnetic data assimilation. Nonlinear Processes Geophys. 19, 365–382.
Morzfeld, M., Tu, X., Atkins, E., Chorin, A., 2012. A random map implementation of implicit filters. J. Comput. Phys. 231, 2049–2066.
Nozières, P., 1978. Reversals of Earth's magnetic field: an attempt at a relaxation model. Phys. Earth Planet. Inter. 17, 55–74.
Olson, P., Driscoll, P., Amit, H., 2009. Dipole collapse and reversal precursors in a numerical dynamo. Phys. Earth Planet. Inter. 173 (1), 121–140.
Olson, P., Deguen, R., Hinnov, L.A., Zhong, S., 2013. Controls on geomagnetic reversals and core evolution by mantle convection in the phanerozoic. Phys. Earth Planet. Inter. 214, 87–103.
Pétrélis, F., Fauve, S., 2008. Chaotic dynamics of the magnetic field generated by dynamo action in a turbulent flow. J. Phys.: Condens. Matter 20, 494203.
Pétrélis, F., Fauve, S., Dormy, E., Valet, J.-P., 2009. Simple mechanism for reversals of Earth's magnetic field. Phys. Rev. Lett. 102, 144503.
Rikitake, T., 1958. Oscillations of a system of disk dynamos. Math. Proc. Cambridge Philos. Soc. 54, 89–105.
Sarson, G.R., Jones, C.A., 1999. A convection driven geodynamo reversal model. Phys. Earth Planet. Inter. 111 (1), 3–20.
Sun, Z., Tangborn, A., Kuang, W., 2007. Data assimilation in a sparsely observed one-dimensional modeled MHD system. Nonlinear Processes Geophys. 14, 181–192.
Talagrand, O., Courtier, P., 1987. Variational assimilation of meteorological observations with the adjoint vorticity equation. I: Theory. Q. J. R. Meteorolog. Soc. 113 (478), 1311–1328.
Valet, J.-P., Fournier, A., 2016. Deciphering records of geomagnetic reversals. Rev. Geophys. 54 (2), 410–446. 2015RG000506.
Valet, J.-P., Meynadier, L., Guyodo, Y., 2005. Geomagnetic field strength and reversal rate over the past 2 million years. Nature 435, 802–805.
van Leeuwen, P., 2009. Particle filtering in geophysical systems. Mon. Weather Rev. 137, 4089–4144.
Wicht, J., Meduri, D., 2016. A Gaussian model for simulated geomagnetic field reversals. Phys. Earth and Planet. Inter. 259, 45–60.
Ziegler, L.B., Constable, C.G., Johnson, C.L., Tauxe, L., 2011. PADM2M: a penalized maximum likelihood model of the 0–2 Ma paleomagnetic axial dipole model. Geophys. J. Int. 184 (3), 1069–1089.